Separating the impact of individual land surface properties on the terrestrial surface energy budget in both the coupled and un-coupled land-atmosphere system

Marysa M. Laguë*

University of Washington Department of Atmospheric Sciences, Seattle, WA, USA

Gordon B. Bonan

National Center for Atmospheric Research, Boulder, CO, USA

Abigail L. S. Swann

University of Washington Department of Atmospheric Sciences and Department of Biology, Seattle, WA, USA

This article is a preprint published at EarthArXiv

*Corresponding author address: Marysa M. Laguë, University of Washington Department of Atmospheric Sciences, Box 351640, Seattle WA, 98195, USA
E-mail: mlague@uw.edu

ABSTRACT

Changes in the land surface can drive large responses in the atmosphere on local, regional, and global scales. Surface properties control the partitioning of energy within the surface energy budget to fluxes of shortwave and longwave radiation, sensible and latent heat, and ground heat storage. Changes in surface energy fluxes can impact the atmosphere across scales through changes in temperature, cloud cover, and large-scale atmospheric circulation. We test the sensitivity of the atmosphere to global changes in three land surface properties: albedo, evaporative resistance, and surface roughness. We show the impact of changing these surface properties differs drastically between simulations run with an offline land model, compared to coupled land-atmosphere simulations which allow for atmospheric feedbacks associated with land-atmosphere coupling. Atmospheric feedbacks play a critical role in defining the temperature response to changes in albedo and evaporative resistance, particularly in the extra-tropics. More than 50% of the surface temperature response to changing albedo comes from atmospheric feedbacks in over 80% of land areas. In some regions, cloud feedbacks in response to increased evaporative resistance result in nearly 1K of additional surface warming. In contrast, the magnitude of surface temperature responses to changes in vegetation height are comparable between offline and coupled simulations. We improve our fundamental understanding of how and why changes in vegetation cover drive responses in the atmosphere, and develop understanding of the role of individual land surface properties in controlling climate across spatial scales – critical to understanding the effects of land-use change on Earth's climate.

1. Introduction

While it is intuitive to think about how climate impacts the land surface, here we focus on how changes in the land surface influence the climate system. In particular, we focus on the effects of changing land surface properties associated with vegetation change. The effects on climate of changing vegetation vary depending on the location of the vegetation change.

For example, tropical forests have high rates of transpiration, and thus high rates of evaporative cooling; tropical deforestation reduces this evaporative cooling effect, leading to warming at the surface (Bonan 2008b). Increasing tree cover in the mid-latitudes has been shown to alter climate locally by warming and reducing cloud cover (Swann et al. 2012; Laguë and Swann 2016). Changes in vegetation at high latitudes can modify surface temperatures through both surface albedo and atmospheric water vapor changes (Bonan 2008b; Swann et al. 2010). The effects of historical land-use and land cover change have been shown to impact near-surface air temperatures and energy fluxes (Pitman et al. 2009; De Noblet-Ducoudré et al. 2012), while future land use has been proposed as a potential method of mitigating anthropogenic climate change (Canadell and Raupach 2008). In addition to directly influencing surface fluxes and temperature, interactions between vegetation change and the atmosphere can drive atmospheric feedbacks and global-scale teleconnections which further influence surface climate, both locally and remotely (Bonan 2008b; Swann et al. 2012; Laguë and Swann 2016; Kooperman et al. 2018).

Vegetation change has been observed to drive changes in surface energy fluxes across a range of biomes (Lee et al. 2011). In addition to observational studies, much of our understanding of land-atmosphere coupling and vegetation-climate feedbacks comes from models of Earth's land-atmosphere-ocean-sea ice system. Land surface models represent the biogeophysical coupling between the land and atmosphere through fluxes of momentum, energy, and water, which are in turn modulated by the land surface albedo, rates of evapotranspiration, and aerodynamic surface roughness. The climate at the land surface is determined both by the background regional climate as well as the characteristics of the local land surface; changes in individual land surface properties each have a different impact on surface temperature and energy fluxes. Albedo directly controls the amount of solar energy absorbed by the surface; aerodynamic roughness controls the efficiency of turbulent energy exchange with the atmosphere; and the resistance to evapotranspiration controls how much water can move from the land surface to the atmosphere. Changes in vegetation modify each of these surface properties in different ways, and changes in different properties of the land surface drive changes in the surface energy budget and surface temperatures. Through these changes in energy fluxes, the land can drive changes in the atmosphere, ranging from small local changes in air temperatures or cloud cover to large, global-scale changes in circulation (Devaraju et al. 2018).

Surface energy fluxes are the complex outcome of biogeophysical processes at the land surface, with changes in any individual surface property having a different effect on climate. In modern Earth System Models, it is often difficult to individually perturb a single land surface property. In a model such as the Community Land Model (CLM, (Lawrence et al. 2018)), surface albedo is the complex result of leaf and stem reflectance and transmittance, the orientation of leaves, the amount of leaf and stem material, interception of snow in the canopy, soil color, soil moisture, and snow cover. Evaporation is calculated from stomatal conductance for transpiration, a conductance for soil evaporation, and evaporation of intercepted water held externally on foliage. Stomatal conductance itself depends on photosynthetic rates as determined by the photosynthetic capacity of the canopy as modified by light absorption, temperature, vapor pressure deficit, soil moisture availability, and atmospheric CO_2 concentration. Because of these complex relationships, many seemingly simple properties of a land surface model, such as albedo, are actual emergent properties of the model. As such, it is difficult to directly prescribe a change in a specific surface property such as albedo or evaporative resistance, or anticipate how a change in vegetation type may actually influence these surface properties. Davin et al. (2010) isolated the individual effects of albedo, evaporative resistance, and surface roughness when comparing the climate effects of forests versus grasslands using the ORCHIDEE land model, but such a modeling protocol is uncommon. Alternatively, using climate models with imposed vegetation change, or a mix of linearized surface energy budget equations and flux tower observations, the relative contribution of different surface fluxes to changes in surface temperatures can be estimated (Lee et al. 2011; Boisier et al. 2012).

The effects of human-induced land use and land cover change can vary largely between different land-atmosphere models, as shown by the LUCID experiments (Pitman et al. 2009; De Noblet-Ducoudré et al. 2012). These differences come in large part from the different ways various models represent complex land surface properties. Here, we focus explicitly on testing the sensitivity of the climate system to three land surface properties in a single land-atmosphere model.

Modifying surface energy fluxes through vegetation change has a direct impact on surface climate. Independent of interactions with the atmosphere, repartitioning surface energy fluxes on the land surface can modify surface temperatures and water availability. Land-atmosphere coupling with the near-surface atmosphere further modifies the effect of a change in some land surface property on surface temperatures and energy fluxes. For example, Vargas Zeppetello et al. (2019) discuss the coupling between surface temperatures, lower atmospheric temperatures, and downwelling longwave radiation reaching the land surface, while Dirmeyer (2001) identify regions with strong coupling between the land surface state and lower atmospheric temperatures, humidity, and even precipitation.

In addition to local, near-surface land-atmosphere coupling changes in response to changes in the land surface, larger-scale changes in the atmosphere can also occur in response to land surface changes, which can then feed back on surface climate, both locally and remotely. For example, modifying forest cover in the mid-latitudes can alter mid-latitude cloud cover, which in turn modifies the amount of sunlight reaching the land surface (Laguë and Swann 2016). Vegetation can also modify local precipitation (Kooperman et al. 2018), or remote precipitation by driving changes in large-scale circulation (Swann et al. 2012). These large-scale atmospheric feedbacks to vegetation change can result in remote climate and vegetation responses in regions far removed from the initial vegetation change, as a result of changes in large-scale atmospheric circulation (Swann et al. 2012; Garcia et al. 2016; Laguë and Swann 2016; Swann et al. 2018). Analysis of the climate impact of changes in vegetation which do not allow for atmospheric feedbacks, such as simulations of changes in vegetation forced with non-interactive data atmospheres (e.g. land models forced with reanalysis) capture the direct surface climate response, but are unable to capture any of the climate response to vegetation change resulting from atmospheric feedbacks.

Changes in vegetation have been shown to drive substantial atmospheric responses in many modern ESMs (Gibbard et al. 2005; Bala et al. 2007; Davin et al. 2010; Chen et al. 2012; Medvigy et al. 2013; Devaraju et al. 2015; Badger and Dirmeyer 2015; Swann et al. 2012; Laguë and Swann 2016). However, as mentioned above, changing vegetation type in a modern land model encompasses many simultaneous changes to multiple land surface properties; several studies using early coupled global climate models demonstrated the ability of changes in *individual* surface properties to influence global climate, including albedo (Charney et al. 1975; Charney 1975; Charney et al. 1977), roughness (Sud et al. 1988), and land evaporation (Shukla and Mintz 1982).

In this study, we introduce an idealized land model, the Simple Land Interface Model (SLIM), which we couple to a modern Earth System Model. We use this idealized land model to examine the effects of specified changes in vegetation albedo, evaporative resistance, and surface roughness in uncoupled land-only and in coupled land-atmosphere simulations. These simulations examine climate sensitivities to specific land surface processes, identify different regional climate responses, quantify the impact of atmospheric feedbacks from land surface changes, and provide a quantitative evaluation of how large a surface perturbation is required to achieve a desired change in surface temperature.

2. Methods

a. Experimental Design

In order to modify a single land surface property, while holding all other properties fixed, we wrote a very simple land surface model (see section b), which can be coupled to the Community Earth System Model (CESM (Hurrell et al. 2013)). This simple land model replaces the Community Land Model v. 5 (CLM5; (Lawrence et al. 2018)) within CESM. Simulations are run coupled to the Community Atmosphere Model v. 5 (CAM5) or forced by an atmospheric dataset; a slab ocean model (SOM) (Neale et al. 2012); and the Los Alamos Sea Ice Model for interactive sea ice (CICE5) (Hunke et al. 2013; LANS 2017). The slab ocean assumes ocean circulation does not change throughout the simulation (monthly heat fluxes are prescribed for each ocean gridcell, representing horizontal and vertical energy transport within the ocean), but allows sea surface temperatures (SSTs), and thus energy exchange with the atmosphere, to adjust to forcings from the atmosphere. SOMs allow atmospheric signals to propagate further than fixed SST models, by allowing ocean temperatures to respond to changes in energy fluxes from the atmosphere, but are much less computationally expensive than fully dynamic ocean models and don't allow for climate signals driven by variability in ocean circulation. As such, the SOM provides a good compromise for studying the impacts of changes in the land surface on atmospheric circulation. The role of oceans in propagating land surface change impacts on global climate has been previously demonstrated (e.g. Bonan et al. (1992); Davin et al. (2010); Swann et al. (2012)); here we capture some of that response by allowing sea surface temperatures and sea ice to change, but do not capture any response relating to changes in ocean circulation or heat capacity.

In each experiment, we modify the value of a single surface property while holding the rest of the surface properties fixed. For each surface property, we run two sets of simulations: one where the land model is forced with a data atmosphere ('offline'), and one running fully coupled to CAM5 (figure 1). Land models are frequently run offline (that is, not coupled with an interactive atmosphere); here, we are interested in identifying how imposing the same changes on the land surface model both offline and coupled to an interactive atmosphere impact the resulting surface energy fluxes and temperatures in response to the change in the land surface. Other delineations of the land-atmosphere boundary, such as allowing the land to interact with a boundary layer but not a larger-scale atmosphere, would result in a different interpretation of the role of atmospheric coupling.

In the offline simulations, we use atmospheric forcing data generated by a control simulation of CAM5 running coupled to the simple land model with the following surface property values over all non-glaciated land regions: snow-free albedo = 0.2, evaporative resistance = 100 s/m, and vegetation height = 0.1 m. These values were chosen as they roughly correspond to a world where all non-glaciated lands are grasslands. The offline simulations are all forced with the same 3-hourly atmospheric forcing data saved from the last 30 years of this coupled simulation (where the first 20 years are discarded to allow the model to reach equilibrium). We find the results to be qualitatively similar (that is, the direction and magnitude of the response of surface temperature and energy fluxes to a change in surface property is the same) when the offline simulations are forced with GSWP3 (Global Soil Wetness Project, Phase 3; `http://hydro.iis.u-tokyo.ac.jp/GSWP3/`)

reanalysis (Compo et al. 2011), which is the standard atmospheric forcing dataset used to evaluate CLM5 in offline simulations (Lawrence et al. 2018).

We perturb the value of each of these surface properties over all non-glaciated (in the present day) land surface (table 1). For albedo α, we use $\alpha = 0.1$ (comparable to the albedo of a needleleaf evergreen forest), $\alpha = 0.2$ (comparable to the albedo of a grassland), and $\alpha = 0.3$ (comparable to the albedo of a desert) (Bonan 2008a), while holding evaporative resistance fixed at 100 s/m and vegetation height fixed at 0.1 m. For evaporative resistance r_s, we use $r_s = 50 s/m$ (low resistance, comparable to that of a crop like wheat), r_s = 100 s/m , and r_s = 200 s/m (moderately high resistance, comparable to that of a pine forest - see Fig. 17.10 in Bonan (2015)), while holding albedo fixed at 0.2 and vegetation height fixed at 0.1 m. For vegetation height h_c (height of canopy) we use $h_c = 0.1$ m (short grassland), h_c=1.0 m (tall grass), h_c = 2.0 m (shrub/short tree) (Bonan 2008a). After approximately 2 m of vegetation height, the response of surface temperatures and energy fluxes to subsequent increases in vegetation height becomes much shallower; as such, we perform an additional three experiments with h_c = 5.0 m, h_c = 10.0 m, and h_c = 20.0 m, to explore the response of surface fluxes to a range of tree heights; these results are presented in the supplement, while here we focus on the 0.1-2.0 m range of vegetation heights.

While the goal of this study was to separate the atmospheric sensitivity to individual surface properties which often change simultaneously as a result of vegetation change, there are situations where real-world vegetation change only modifies one of these properties. An example of this is the stomatal response of vegetation to changes in atmospheric water demand, which would modify evaporative resistance but not albedo or vegetation height. Specific crop cultivars have been developed to modify water use (e.g. Zhang et al. (2005)), while growing more reflective plants has been proposed as a type of geoengineering (Caldeira et al. 2013). Also, there are other land surface properties not perturbed here which could impact surface energy fluxes over various time scales, included soil heat capacity, which has been shown to impact the diurnal amplitude of surface temperatures (Cheruy et al. 2017).

Each simulation is run for 50 years; we discard the first 20 years of the simulation to allow for the model to reach equilibrium, and evaluate the last 30 years of each simulation. The drift in surface temperatures over the last 30 years, globally averaged, is less than 0.01 K. Simulations are run at a resolution of 1.9° latitude by 2.5° longitude.

b. Simple Land Interface Model (SLIM)

The simple land model used here (the Simple Land Interface Model) allows us to individually modify different surface properties within a coupled climate model, to isolate their effect on climate. SLIM is described in greater detail in the supplemental materials of this paper.

For this study, SLIM was written to couple into CESM in place of CLM. At every land location, the user can independently set each land surface property. These properties include the snow-free albedo, evaporative resistance, vegetation height (for aerodynamic roughness), the capacity of the land to hold water, the heat capacity and thermal resistance of the soil, the number and depth of soil layers, the snow-masking depth (the volume of snow required to mask the snow-free ground albedo), and the locations of glaciers. Heat diffusion through the soil is solved on a discretized vertical grid which is decoupled from the water budget of the land. Hydrology is represented using a bucket model, where the resistance to evaporation from the bucket is a combination of a user-prescribed "lid" resistance (comparable to the bulk stomatal resistance of a complex land model like CLM) and an additional resistance due to how empty the bucket is (as in the GFDL-LM2 model (Milly and Shmakin 2002; Anderson et al. 2004) and Manabe and Bryan (1969)). Given semi-realistic values for albedo, vegetation height, and evaporative resistance, SLIM can produce surface temperatures that differ less than 1K to those from CLM5 over most regions using reanalysis atmospheric forcing data (see supplemental figures 2-9).

At each time step, the land model solves a linearized surface energy budget to calculate a surface temperature and surface fluxes of radiation, sensible and latent heat flux, and heat uptake by the ground. A simple snow model allows snow falling from the atmosphere to accumulate on the surface and mask the bare ground albedo; snow is removed from the surface either by sublimation to the atmosphere, or by melting into the land surface.

c. Analysis Approaches

For each surface property, we fit a least-squares linear regression model of a climate variable (e.g. surface temperature) to the prescribed values of the surface property (figure 2). Each surface property value has 30 points, one annual mean value for each spun-up simulation year. When fitting our linear model, we track how linear the relationship between the change in global surface property (e.g. albedo in figure 2) and the response of the climate variable in question (surface temperature in figure 2) using the r^2 value of the linear relationship. We test if the slope is significantly different from zero using the p value (where $p < 0.05$ indicates a statistically significant relationship at 95% confidence).

In order to evaluate the climate response to physically meaningful changes in each surface property, we scale the slope by a somewhat arbitrary scaling factor chosen to show a maximum temperature change of roughly 1 K in the coupled simulations, which corresponds to maximum surface energy flux changes of approximately 10 W/m^2. This corresponds to a scaling factor of -0.04 for albedo (the surface gets 4% darker), 50 s/m for evaporative resistance (increasing surface resitance), and -0.5 m for vegetation height (response per 0.5 m shorter/smoother the surface becomes). For example, a slope of -20 K per 1.0 increase in albedo isn't physically meaningful, as albedo values only range between 0 and 1. Instead, we scale the slope to get a change of -0.8 K (-20 K$\times$0.04) per 4% decrease in albedo. In order to evaluate the warming impact of each surface property, we look at the effects of *decreasing* albedo, *increasing* evaporative resistance, and *decreasing* vegetation height. This slope value is calculated individually for each gridcell, and presented as the climate response to each scaled change in surface property in the rest of the paper.

In our offline simulations, the impact on surface energy fluxes and temperature of a change in a land surface property represents the response *independent* of any atmospheric response to the change in land surface property. That is, the changes are driven only by the surface energy budget adjustment to the local change in surface property (figure 1a), and not by any change in atmospheric temperature, cloud cover, etc., which may occur due to any interaction with the atmosphere (figure 1b and c). For example, even if the surface energy fluxes on the land surface changed dramatically in response to a change in some surface property, the atmospheric fluxes sent down to the land model would remain the same. Thus, the offline simulations give us an estimate of the direct response of the surface energy budget to a change in the land surface *in isolation* from any atmospheric changes - note that this is more of a theoretical concept, as in the real world, the atmosphere and land are always free to interact.

In comparison, coupled simulations capture the direct surface energy budget response (i.e. the response we would expect in an offline simulation), changes in surface fluxes due to local atmospheric responses to the initial surface change (figure 1b), as well as changes in local surface fluxes due to remotely driven atmospheric responses (i.e., driven by land surface property changes elsewhere; 1c). We call the changes in the atmosphere *driven* by initial changes in land surface properties, which then go on to modify energy fluxes at the land surface, the *atmospheric feedback* to that initial land surface change.

3. Results and Discussion

a. Albedo

The albedo (the fraction of incident radiation that is reflected) of different land surfaces varies greatly between vegetation and land cover types. Coniferous forest albedos range from 0.05-0.15, deciduous forests from 0.15-0.20, grasslands from 0.16-0.26, and soils from 0.05-0.40; snow cover leads to land albedos of over 0.9 (Bonan 2002). We scaled our results so that they are relative to a 0.04 change in land surface albedo; physically, this can be thought of as a conservative approximation of the albedo difference between a coniferous and deciduous forest, or a deciduous forest and a grassland.

Albedo directly controls the amount of solar energy absorbed by the land surface, and as such, plays an important role in controlling land surface temperatures. If the land surface absorbs more energy in response to decreasing surface albedo, more energy must also leave the surface, either by an increase in turbulent energy fluxes (sensible and latent heat), or by an increase in longwave radiation emitted by the surface (increasing surface temperature). Over long timescales the storage of energy by the land surface is negligible.

1) Offline

The differences in the pattern of surface temperature change in response to albedo in the offline simulations, where no atmospheric feedbacks are allowed, are caused by differences in (i) the change in absorbed solar energy (a function of downwelling solar radiation) and (ii) the partitioning of energy into turbulent heat fluxes vs surface heating.

In the offline simulations, the surface temperature response to decreasing land surface albedo is largest in the mid-latitudes, and smallest at high latitudes (figure 3d; supplemental figure 10a).

Because the incident sunlight is weaker at high latitudes, the same decrease in surface albedo results in a smaller net increase in absorbed solar radiation compared to lower latitudes. This means that in high latitudes there is less extra energy that the surface needs to get rid of (either through warming or through turbulent heat fluxes), and the total temperature change is small. Conversely, surface temperature changes in the offline simulations are larger in regions with a large amounts of incident solar radiation at the surface (the tropics and mid-latitudes). Despite the fact that equatorial regions receive the most incoming solar radiation at the top of the atmosphere, the large amount of deep cloud cover over the tropics blocks a lot of solar radiation, and the largest amount of downwelling solar radiation at the surface in the annual mean actually occurs over northern Africa and the Arabian Peninsula (supplemental figure 11).

The surface temperature response to decreasing albedo in the tropics is smaller than in the mid-latitude deserts not only because of the difference in the incident solar radiation at the surface, but also because of differences in the amount of water available on the land surface due to high tropical precipitation rates. As such, though decreasing albedo does lead to an increase in the total energy absorbed at the surface in the tropics (figure 4e), that excess energy is removed from the surface primarily by evaporating more water (figure 4h), negating the need for increased surface temperatures and changes in upwards longwave radiation (figure 4f). The largest surface temperature changes in the offline simulations occur in sunny, dry regions such as the Sahara and Arabian Peninsula where latent cooling is not able to occur and the excess absorbed solar energy is balanced by increased surface temperatures and sensible heat fluxes (figure 4f, g).

2) Coupled

Rather, changes in energy fluxes would be transmitted to the atmosphere, with potential resulting interactions and feedbacks between the land and the atmosphere. Interactions with the atmosphere could cause further changes in surface climate through several pathways, three of which are discussed here. First, changes in atmospheric air temperature could modify the magnitude of downwelling longwave radiation and the surface-to-atmosphere temperature gradient which influences sensible heat flux. Second, changes in cloud cover could modify the magnitude of both downwelling shortwave and longwave radiation at the surface. Third, changes in humidity could modify the vertical moisture gradient which influences latent heat flux.

In the coupled simulations, not only is the response of surface temperature to decreasing albedo much larger in magnitude compared with the offline simulations, but it is also drastically different in spatial pattern (figure 3a vs d). Rather than the high latitudes having the smallest surface temperature response to decreased albedo, they now have some of the largest warming signals (along with hot, dry regions in the mid-latitudes). The magnitude of warming at the surface in the coupled simulations is larger than in the offline simulations in almost all regions, with the exception of equatorial Africa. When the atmosphere is allowed to respond (coupled simulations), decreasing the surface albedo still generally leads to an increase in absorbed shortwave radiation. However, the change in absorbed energy is smaller in magnitude and has a different spatial pattern than in the offline simulations, with near-zero changes in absorbed shortwave radiation in the parts of the tropics and high latitudes, and the largest increases in absorbed solar radiation occurring over the mid-latitudes and parts of tropical South America (compare figure 4a and d). Surprisingly, there are some locations where decreasing albedo actually leads to slightly less absorbed solar radiation at the surface. This response is most notable in the coupled simulation over equatorial Africa, and is the result of increased cloud cover over this region reducing the incident solar radiation (supplemental figure 12).

Across the tropics, decreasing albedo leads to much larger increases in latent heat flux in the coupled simulations than in the offline simulations, most notably over India, equatorial Africa, Indonesia, and the western Amazon (figure 4 d). Many of these regions also stand out as having a *decrease* in net longwave radiation at the surface with decreased albedo, despite surface warming (figure 4 b). Surface warming is accompanied by an *increase* in upwards longwave radiation emitted from the surface, following the Stefan-Boltzmann equation $LW^{\uparrow} \propto \sigma T_s^4$ (where T_s is the radiative skin temperature of the land surface, and σ is the Stefan-Boltzmann constant). However, when the atmosphere warms in response to surface warming, there is also an *increase* in downwards longwave radiation at the surface; thus, more energy is being input to the land system as a result of a warmer atmosphere (Vargas Zeppetello et al. 2019). The net longwave radiation at the surface is the difference between the longwave radiation emitted upwards, and the downwelling longwave radiation reaching the surface from the atmosphere. In some locations, the increases in upwards longwave radiation (corresponding to increases in surface temperatures) are larger than the increases in downwelling longwave radiation (corresponding to a warmer atmosphere), resulting in decreased *net* longwave radiation at the surface as albedo decreases.

The increase in annual mean surface temperature at high latitudes is largest in autumn and winter (not shown), when the incoming insolation is very small. This is surprising, as decreasing surface albedo during dark months has a much smaller impact on absorbed shortwave radiation than decreasing albedo during bright months; moreover, much of the high-latitude land surface is covered with (bright) snow during the winter months, masking the direct change in surface albedo. This suggests that the high-latitude winter warming is not locally driven. Indeed, there is a significant increase in energy transport into the Arctic region from the mid-latitudes (see section *Impact on Global Atmospheric Circulation* below), which should lead to high-latitude warming. Additionally, there significant loss of sea ice (largest in September) for the reduced albedo simulations, which is likely due to a combination of increased energy transport to the Arctic and local warming from summer albedo changes triggering an ice-albedo feedback.

b. Evaporative Resistance

Vegetation can directly control the evaporative resistance of a surface through the opening and closing of stomata on their leaves. The evaporative resistance of a surface is also controlled by soil properties, vegetation root depth, and how much water is available in the soil. Here, we present results for a 50 s/m change in the evaporative resistance of the land surface. The total resistance to evaporation is a combination of the surface resistance (which we perturb) and the resistance associated with how dry the soil is. Changing the evaporative resistance of the land surface has no direct effect on the total amount of energy absorbed by the surface; rather, it controls the partitioning between latent and sensible heat fluxes (figure 5). In general we expect that a surface with higher resistance would have relatively more sensible and less latent heat flux, leading to higher surface temperatures relative to a surface with lower resistance.

1) Offline

Our offline simulations show the largest change in surface temperature in the wettest regions of the tropics (figure 3e). This response is intuitive: increasing resistance in these regions causes a large reduction in latent heat flux (figure 5h), which is compensated for by surface warming, increased sensible heat flux, and increased upwards longwave radiation (figure 5f, g). Dry regions (e.g. the Sahara and central Australia) have no temperature response to increasing surface resistance in the offline simulations: these regions have very little water on the land surface and near-zero latent heat fluxes, so making it more difficult to evaporate water does not result in any substantial changes to the actual magnitude of latent heat flux, and thus there is no compensating change in the other terms of the surface energy budget. The amount of shortwave radiation absorbed at the surface is only a function of the downwelling shortwave radiation and the albedo of a surface; as such, increasing evaporative resistance in offline simulations has no impact on the absorbed solar energy at the surface (figure 5e). Instead, evaporative resistance directly controls the partitioning of energy between turbulent heat fluxes, with the largest temperature responses occurring in warm locations with large amount of water available to evaporate, such as Indonesia and the coastal regions of the Amazon (figure 5h). These regions have large latent heat fluxes in the mean state, because of a combination of plenty of precipitation (thus lots of water available to evaporate), and plenty of energy entering the land system. Thus, increasing evaporative resistance leads to large magnitudes of change in latent heat fluxes; energy that formerly was used for evaporation instead results in surface heating.

2) Coupled

As with albedo, the pattern and magnitude of the surface temperature response to increasing evaporative resistance over land have a larger magnitude and a spatially distinct pattern in our coupled simulations compared to their offline counterparts (figure 3b). Rather than in the wettest tropical regions, our coupled simulations have the largest changes in surface temperature in response to decreasing surface resistance in the mid-to-high latitudes. Dry regions in the subtropics have the smallest change in surface temperature when evaporative resistance is increased, but these regions still show more warming than in the offline simulations. Though temperature changes in the tropics are small, the decreases in latent heat flux in the wettest regions of the tropics, such as the Maritime Continent, are the largest of anywhere on the globe.

One of the largest changes in surface temperature in response to increased evaporative resistance occurs over southeastern North America. Over this region, there is a slight decrease in evaporation in both the coupled and offline simulations (compare figure 5d and h). However, the changes to temperature and energy fluxes are otherwise quite different. In the coupled simulation, increased evaporative resistance at the land surface drives warming and drying of the regional atmosphere.

The warming and drying of the lower troposphere in this region leads to a decrease in relative humidity and a decrease in low cloud cover (not shown). The reduction in cloud cover in turn allows more solar radiation to reach the surface, causing surface temperatures to rise. Averaged over the region from 85 to 100° W and 32 to 45 °N, a 50 s/m increase in evaporative resistance leads to a 6.2 W/m^2 in absorbed solar radiation in the coupled simulations. This increase in energy into the land system over this region results in a temperature increase of roughly 0.9 K in the coupled simulation, compared to a warming of only 0.2 K in the uncoupled simulation (per 50 s/m increase in evaporative resistance). This cloud feedback is particularly interesting as evaporative resistance cannot directly modify the amount of energy absorbed by the surface.

The decreases in latent heat flux in response to increased evaporative resistance are actually smaller in the coupled simulations than in the offline simulations. This is because in the coupled simulations, as the air dries in response to reduced evaporation, the atmospheric demand for water increases.

c. Roughness

1) OFFLINE

Changing the height of vegetation changes the aerodynamic roughness of the land surface, and thus how effectively turbulent energy fluxes can be exchanged with the atmosphere. Decreasing surface roughness makes it harder to remove energy from the land surface by turbulent mixing, but has no direct impact on the total amount of energy entering the land system (figure 6e). Decreasing the roughness leads to a reduction in sensible heat flux, balanced by a corresponding increase in longwave radiation, with little to no impact on latent heat flux (figure 6f-h).

The strongest impacts on surface energy fluxes occur in regions with large sensible heat fluxes, such as the sub-tropical desert regions. Note that the pattern of temperature response is similar for both the short and tall regime of changes in vegetation heights, but that the height change required to scale responses to roughly 1K shifts from 0.5 m in the short regime to 10.0 m in the tall regime (see supplemental figure 16 and further discussion in the supplement). This reflects a shift in how efficiently a given change in surface aerodynamic roughness can impact energy fluxes and surface temperatures - when the land is relatively smooth, small changes in aerodynamic roughness are important; when the land is relatively rough, small changes have little impact.

2) Coupled

Unlike decreasing albedo and increasing evaporative resistance, which result in larger surface temperature changes with different spatial patterns in the coupled compared to the offline simulations, decreasing surface roughness results in a similar pattern and magnitude of warming in the coupled vs offline simulations (figure 3c, f). Also unlike the albedo and evaporative resistance cases, which modify both the surface temperature (radiative skin temperature) and the air temperature in the coupled simulations, the temperature response in the coupled roughness simulations is primarily restricted to the surface itself (figure 7).

In both the offline and coupled experiments, decreasing the vegetation height (and thus the surface roughness) has the largest impact on temperature in the warmest regions of the globe, with much smaller annual mean temperature increases in the high latitudes. As the roughness of a surface should impact how efficiently turbulent heat can be moved away from the surface, it should have the largest impact on surface temperatures in regions where turbulent heat fluxes play a large role in balancing the surface energy budget.

d. *Feedbacks*

In the real world, as well as in our coupled simulations, the land surface does not respond to forcing in isolation – changes in surface energy fluxes are communicated to the atmosphere, and can drive changes in atmospheric temperature, humidity, cloud cover, and circulation as noted above. Many of these atmospheric responses to changes in surface energy fluxes can then feedback on the surface energy budget itself. For example, a change in cloud cover driven by some initial surface change could lead to a subsequent change in solar radiation reaching the surface, which in turn drives further changes in the surface energy budget (figure 1b). Additionally, the atmosphere can transmit information (e.g. changes in circulation, or fluxes of water, heat, or clouds) from one atmospheric column to another, such that a change in the land surface in one region can, through these remote atmospheric feedbacks, influence the surface energy budget in a remote region (figure 1c).

1) Total Atmospheric Feedback

The differing surface fluxes between simulations where the atmosphere is or is not allowed to respond result in remarkably different patterns and magnitudes of surface temperature change for the same imposed surface property change as described above. Because the atmosphere can respond to changes in surface fluxes, modifying land albedo, evaporative resistance, and roughness can lead to large changes in cloud cover, snow fall, sea ice, and energy transport, all of which can feedback on the surface energy fluxes over the land surface.

We define the total *atmospheric feedback* on surface climate to be the difference between the coupled simulation and the offline simulation (figure 8 – for surface air temperature, this would be the difference between the left and right columns of figure 3). For albedo and evaporative resistance, the extra-tropics have up to 1K of additional surface warming when the atmosphere is allowed to respond to changes in surface energy fluxes driven by the modified land surface properties.

To identify the strength of the atmospheric feedback – that is, what percent of the total warming signal comes from interactions with the atmosphere – we calculate the percent change in a surface temperature between the coupled simulation and the offline simulation:

$$\text{Feedback Strength} = \frac{\text{coupled} - \text{offline}}{|\text{coupled}|} \times 100. \tag{1}$$

For albedo, over 50% of the change in surface temperature comes from interactions with the atmosphere over more than 80% of global, non-glaciated land area, with as much as 75% of the temperature response coming from the atmosphere over 28% of land area. This is even larger for evaporative resistance, over 50% of the surface temperature increase comes from atmospheric feedbacks over 84% of non-glaciated land areas, with increases as large as 75% over 64% of land area (figure 9). This suggests that vegetation changes which significantly alter either the color of the land surface, or how difficult it is to remove water from the land surface (such as the conversion of a forest to a grassland) have significant impacts on surface climate *due to* changes in the atmosphere in response to the initial vegetation change.

2) Impact on Global Atmospheric Circulation

In addition to changes in temperature driven by changes to the local surface energy budget, decreasing albedo and increasing evaporative resistance both drive changes in large-scale atmospheric circulation. A northward shift of the Haley circulation results in a significant change in northward energy transport by the atmosphere (figure 10a). When excess energy is absorbed in the northern hemisphere the Hadley Circulation shifts to move energy from the energy-rich northern hemisphere to the southern hemisphere, causing the intertropical convergence zone to shift towards the energy rich hemisphere (figure 10b). This response is well documented in slab ocean models (Chiang and Bitz 2005; Kang et al. 2008; Swann et al. 2012; Frierson and Hwang 2012; Chiang and Friedman 2012; Laguë and Swann 2016) and also found in models with dynamical oceans (Broccoli et al. 2006). If such an energy gradient is established, we expect to see this large-scale circulation response.

In the case of albedo, a darker surface directly increases the amount of energy absorbed by the land surface. Because the northern hemisphere has more land – in particular, more non-glaciated land (we only modify non-glaciated land in this study) – than the southern hemisphere, decreasing land albedo globally results in more energy being absorbed by the surface in the northern hemisphere than in the southern hemisphere. The resulting energy gradient causes a southward shift in the Hadley Circulation, evident in the increased southward energy transport across the equator. However, decreasing land albedo also has the effect of slightly increasing the energy transport from the northern mid-latitudes into the Arctic, leading to high-latitude warming *driven* by the non-local albedo changes in the tropics and mid-latitudes.

Evaporative resistance, unlike albedo, does not directly change the amount of energy absorbed by the surface – rather, it changes the partitioning of energy between sensible and latent heat. As such, it is surprising that increasing evaporative resistance drives a large, significant decrease in northward energy transport (blue line in figure 10a). We find that increasing evaporative resistance drives a decrease in cloud cover over many land areas; this causes an increase in downwelling shortwave radiation at the surface, and thus an increase in net shortwave energy absorbed at the surface despite no change in surface albedo (supplemental figure 12b, figure 5a). This introduces the hemispheric energy imbalance required to drive the observed large-scale shifts in energy transport.

Changing the roughness of the surface has only a weak impact on the total amount of energy absorbed by the land, and as such we see only small changes in northward energy transport and zonal mean precipitation (orange lines in figure 10).

3) Response over oceans

Changes in land surface properties drive changes in surface climate not only over the land, but also over the oceans. The slab ocean model employed in these simulations allows sea surface temperatures (SSTs) and sea surface energy fluxes to respond to changes in the atmosphere (though heat transport within the ocean is held fixed). As such, atmospheric signals *driven by changes in the land surface* can propagate over the oceans, impacting SSTs, oceanic clouds, and precipitation, and potentially reaching far-removed land surfaces. Unlike the climate response over land regions in the fully coupled simulations, where the change in climate may be coming directly from the change in the land surface at that grid cell, or from atmospheric responses to remote changes in the land surface, the climate response over the ocean must inherently be a remote response to changes in the land surface, given that the ocean surface was not directly modified in any of our simulations.

When we make the land surface darker (reduce albedo), there is a large warming response over the Arctic Ocean, caused by a strong sea ice feedback where arctic warming leads to loss of sea ice, which amplifies high-latitude warming (figure 7). The warming which initially drives the sea ice loss is a combination of both local warming from land in the northern high-latitudes, as well as from an increase in energy transport into the high northern latitudes (figure 10a). With a darker land surface, the increase in absorption of solar radiation over land drives increased air temperatures over land; this warming is then advected by the atmosphere, resulting most notably in increased SSTs downwind of land masses in the northern hemisphere. In contrast to the northern hemisphere warming over the oceans, in the southern hemisphere the temperature response over the cloud decks west of South America, southern Africa, and Australia are near-zero or negative. This cooling is caused by an increase in low cloud cover over these regions, which in turn is supported by increase subsidence over these low cloud decks (supplemental figure 15). Whether the increased subsidence is due to the direct albedo change of the neighboring continent (e.g. setting up a local East-West, Walker-like circulation), or is driven by the changes in large-scale atmospheric circulation (e.g. increased subsidence as a result of a shifting ITCZ), would require further simulations and is not the focus of this study.

e. Inverse relationship

Thus far, we have considered the response of various climate variables (e.g. T_s, the surface energy budget, clouds) as the change in that climate variable per incremental change in the magnitude of a surface property (albedo, evaporative resistance, or roughness); that is, we have considered the slope $\frac{\partial \text{atm}}{\partial \text{lnd}}$. However, in order to compare the relative impact of changes in different surface property types it would be useful to know how much of a change in each property is needed to cause the same amount of temperature response. We can use our simulations to consider the inverse relationship $\frac{\partial \text{lnd}}{\partial \text{atm}}$. By scaling $\frac{\partial \text{lnd}}{\partial \text{atm}}$ such that $\partial \text{atm} = 0.1$ K , this relationship can be interpreted as the magnitude of global change in some surface property (albedo, evaporative resistance, or roughness) required to drive a 0.1 K increase in surface temperature at any particular location (figure 11). A similar calculation can be applied to the offline simulations, which *do not account* for any atmospheric feedbacks; in that case, we calculate the local change in surface albedo required to drive an 0.1 K change in local surface temperature, with no interaction effects from the local atmosphere, and no temperature effects from remote albedo change.

In the coupled simulations, only an 0.01 (1%) decrease in global land surface albedo is required to drive 0.1K of warming over 85.3% of land areas (figure 11a). This is well within the range of actual surface albedo changes associated with vegetation change, with grass albedos alone ranging from 0.16-0.26 (Bonan 2002). In the offline simulations, only 14.9% of land areas achieve an 0.1K warming with a 1% decrease in global land albedo (figure 11d).

To achieve an 0.1K temperature increase at any given location from global-scale changes in evaporative resistance, much larger changes in evaporative resistance are required in the offline vs the coupled simulations (figure 11b,e). For example, to see 0.1K of warming over southwestern North America, a 5-10 s/m increase in global land evaporative resistance would be required in the coupled simulations, while a change of over 20 s/m would be required in the offline simulations. The offline simulations require much larger changes in global land evaporative resistance to drive an 0.1K local temperature (figure 11e), largely because the warming response to increased evaporative resistance in the coupled simulations is due to changes in cloud cover which don't occur in the offline simulations. Only in some very wet areas, such as Indonesia, does a change in evaporative resistance translate to a substantial temperature change in the offline simulations.

Decreasing global land surface vegetation height by < 0.1m or less leads to 0.1K of surface temperature change across most of the low to midlatitudes, with smaller height changes required in hot, arid regions (figure 11 c, f). In the high latitudes, where the air is frequently warmer than the surface, particularly during winter, it is not clear that decreasing vegetation height in these regions should lead to warming. Because atmospheric feedbacks play a smaller role in the local climate impact of changing vegetation height, the offline map can be interpreted as an indicator of where a local change in surface roughness is likely to result in a substantial change in local surface temperature.

f. Comparison to Davin et al. (2010)

Davin et al. (2010) used a global climate model to explore the effects of global deforestation. Our results are consistent with Davin et al. (2010) in that increases in global land surface albedo lead to global-scale cooling; the largest temperature changes in their study occur at high latitudes, while our largest temperature changes occur in mid-latitudes. Additional differences could result both from the spatially non-uniform surface changes used in Davin et al. (2010), from the fact that they used a fully dynamic rather than slab ocean, as well as from model-dependency of results. Our work builds upon Davin et al. (2010) in two notable ways: first, by exploring the scaling relationship between different magnitudes of change in albedo, evaporative resistance, or vegetation height and the resulting climate effect, and second, by quantifying how much of the climate response to global changes in each land surface property was the result of atmospheric feedbacks.

g. Caveats and Limitations

In this study we have established that the feedbacks from the atmosphere are large, comprising for example 75% or more of the total response of surface temperature to a change in surface resistance over 64% of land area. However, atmospheric feedbacks can be local (a change in the atmosphere above some location due to a change in land properties at that location) or remote (a change in the atmosphere above some location due to a change in land properties at a different location). We can see this effect clearly over the oceans where the climate response must be entirely remote, as the surface of the ocean is never directly modified in this study. However with our simulations alone, we cannot fully separate the effects of local vs. remote atmospheric feedbacks over land because all land areas are perturbed at the same time; doing so will be left for future studies.

We present the response of surface fluxes and radiative skin temperatures to changes in different land surface properties. It is also important to consider how changes in each surface property impact near-surface air temperature, as this is the temperature humans experience from day-to-day. In the case of albedo and evaporative resistance, the 2m air temperature is only slightly damped compared to the radiative skin temperatures (figure 7 a,b; d,e). However, the change in the 2m air temperature does not necessarily mirror the change in the *surface* (radiative) temperature of the land surface. This is particularly evident when comparing the effect of changes in roughness on surface vs 2m air temperature (figure 7c,f); while albedo and evaporative resistance result in warming both of the land surface and the air in the coupled simulations, the magnitude of surface temperature response to decreasing roughness is much larger than that of 2m air temperature.

In this study we aim to isolate the effect of individual surface properties on climate, and so in each experiment we modify a single land property at a time. When considering the climate impact of actual land use change, for example changing from a forest to a grassland, multiple properties of the land surface are changed simultaneously. It is possible that modifying multiple surface properties at the same time and in different patterns leads to non-linear responses which we have not addressed in the results presented here, but are an area for future study. Identifying which surface property dominates when all the surface properties associated with a given change in vegetation is especially important, given this uncertainty is one of the main reasons vegetation change drives different responses across models (Pitman et al. 2009; De Noblet-Ducoudré et al. 2012). Additionally, the strength of the atmospheric feedbacks presented here are the results of a single atmospheric model (CAM5); other atmospheric models could show stronger or weaker responses to changes in the land surface, particularly with regards to cloud cover. In particular, the strong response of low cloud cover to changes in evaporative resistance from the land surface is likely to be highly dependent on the shallow convection scheme used; the CAM5 model used in this study uses the University of Washington Shallow Cumulus Parameterization (Park and Bretherton 2009; Neale et al. 2012).

4. Summary and Conclusions

We evaluated the sensitivity of the land surface energy budget and land surface temperatures to changes in three individual land surface properties (albedo, evaporative resistance, and aerodynamic roughness). Changes in land albedo result in more absorbed incoming shortwave radiation, which leads to large surface temperatures changes in water-limited regions; temperature changes are small, but changes in latent heat flux are large, in regions with ample terrestrial water availability. Albedo has the largest impact on surface temperatures in warm, sunny regions in the offline simulations, but much larger and spatially broader impacts on surface temperatures across the mid and high latitudes in the coupled simulations due to large-scale interactions with the atmosphere. Changes in evapotranspiration do not directly affect the amount of energy absorbed by the surface; rather, changes in evapotranspiration lead to changes in the partitioning between sensible and latent heat fluxes, with increased surface temperatures and reduced evaporation when evaporative resistance is increased. Changes in evaporative resistance have the largest impact on surface temperature in wet areas such as the tropics in the offline simulations, with even larger surface temperature responses in the coupled simulations in extratropical regions with both wet soil and relatively dry air, such as south-eastern North America and northern Eurasia. Changes in vegetation height modify the aerodynamic resistance of the land surface, and results in a repartitioning of surface energy fluxes between turbulent heat fluxes - mostly sensible heat flux - and emitted surface longwave radiation (corresponding to changes in surface temperature). Changes in surface roughness have the largest impact on surface temperatures in warm, dry regions.

When investigating the climate effect of changes in land surface properties, the results are drastically different between offline land-only simulations driven by non-interactive atmospheric data, and simulations which account for interactions and feedbacks with the atmosphere. The response of surface temperature to changes in albedo and evaporative resistance are much stronger and have a distinctly different pattern in coupled simulations than offline simulations, with over 50% of the total temperature change in response to albedo coming from interactions with the atmosphere in over 80% of land areas. For surface roughness, the pattern and magnitude of temperature change are similar, though not identical, between the coupled and offline simulations. The differences in surface energy flux and surface temperature responses to the same change in the land surface between the coupled and offline simulations come from atmospheric feedbacks responding to surface property-driven changes in surface energy fluxes. These atmospheric feedbacks associated with land-atmosphere coupling include changes in atmospheric temperature, humidity, cloud cover (which go on to modify the amount of solar radiation reaching the surface), and circulation. Some of these circulation responses, such as changes in northward heat transport, are large in spatial scale and thus provide a mechanism for surface property changes in one location to impact climate over far removed land areas.

The inverse relationship presented in this paper describes the change in some land surface property required to produce a change in a given climate variable, for example, the change in albedo required to drive 1K of surface warming at some location. This approach provides a framework to analyze the impacts of land management on different aspects of surface climate. This highlights the importance of accounting for local land-atmosphere interaction impacts on climate, and for quantifying the impacts of remote land use change on the climate of given region when considering the climate impacts of land management in the future.

The simple land model, SLIM, introduced in this paper provides the ideal framework to assess atmospheric responses to prescribed surface perturbations. It allows us to quantify the climate impacts of individual land surface properties while knowing exactly what is changing on the land surface. We foresee this model being useful in applications such as paleoclimate studies where the exact distribution and behavior of vegetation is unknown, studies where the complexity of a modern land surface model is not needed, studies where unexpected feedbacks with complex land dynamics could interfere with the intended experiments, or studies aimed at understanding the behavior of an ESM without complexities in the land surface model.

Acknowledgments. We thank funding support from NSF grant 1553715 to the University of Washington, NSERC grant PGSD3-487470-2016, and the Advanced Studies Program visiting graduate student fellowship at the National Center for Atmospheric Research (2016). We would like to acknowledge high-performance computing support from Cheyenne (doi:10.5065/D6RX99HX) provided by NCAR's Computational and Information Systems Laboratory, sponsored by the National Science Foundation. The SLIM (Simple Land Interface Model) source code is available on github at `https://github.com/marysa/SimpleLand`. The data presented in this paper is available through Research Works, the University of Washington Libraries digital repository, at `http://hdl.handle.net/1773/43463`.

References

Anderson, J. L., and Coauthors, 2004: The new GFDL global atmosphere and land model AM2-LM2: Evaluation with prescribed SST simulations. *Journal of Climate*, **17 (24)**, 4641–4673, doi:10.1175/JCLI-3223.1, URL http://dx.doi.org/10.1175/JCLI-3223.1http://journals.ametsoc.org/doi/abs/10.1175/JCLI-3223.1.

Badger, A. M., and P. A. Dirmeyer, 2015: Climate response to Amazon forest replacement by heterogeneous crop cover. *Hydrology and Earth System Sciences*, **19 (11)**, 4547–4557, doi: 10.5194/hess-19-4547-2015.

Bala, G., K. Caldeira, M. Wickett, T. J. Phillips, D. B. Lobell, C. Delire, and a. Mirin, 2007: Combined climate and carbon-cycle effects of large-scale deforestation. *Proceedings of the National Academy of Sciences of the United States of America*, **104 (16)**, 6550–6555, doi: 10.1073/pnas.0608998104.

Boisier, J. P., and Coauthors, 2012: Attributing the impacts of land-cover changes in temperate regions on surface temperature and heat fluxes to specific causes: Results from the first LUCID set of simulations. *Journal of Geophysical Research Atmospheres*, **117 (12)**, 1–16, doi:10.1029/2011JD017106.

Bonan, G., 2015: *Ecological climatology: concepts and applications*. 3rd ed., Cambridge University Press.

Bonan, G. B., 2002: *Ecological climatology: concepts and applications*. 1st ed., Cambridge University Press.

Bonan, G. B., 2008a: Ecological Climatology: Concepts and Applications, 2nd Edition. *Geographical Research*, **48 (2)**, 221–222, doi:10.1111/j.1745-5871.2009.00640.x, URL http://doi.wiley.com/10.1111/j.1745-5871.2009.00640.x.

Bonan, G. B., 2008b: Forests and climate change: forcings, feedbacks, and the climate benefits of forests. *Science (New York, N.Y.)*, **320 (5882)**, 1444–1449, doi:10.1126/science.1155121, URL http://www.ncbi.nlm.nih.gov/pubmed/18556546http://science.sciencemag.org/content/320/5882/1444.abstract.

Bonan, G. B., D. Pollard, and S. L. Thompson, 1992: Effects of boreal forest vegetation on global climate. *Nature*, **359 (6397)**, 716–718, doi:Doi10.1038/359716a0.

Broccoli, A. J., K. a. Dahl, and R. J. Stouffer, 2006: Response of the ITCZ to Northern Hemisphere cooling. *Geophysical Research Letters*, **33 (1)**, 1–4, doi:10.1029/2005GL024546.

Caldeira, K., G. Bala, and L. Cao, 2013: The Science of Geoengineering. *Annual Review of Earth and Planetary Sciences*, **41**, 231–258, doi:10.1146/annurev-earth-042711-105548.

Canadell, J. G., and M. R. Raupach, 2008: Managing forests for climate change mitigation. *Science*, **320 (5882)**, 1456–1457, doi:10.1126/science.1155458.

Charney, J., W. J. Quirk, S.-h. S.-H. Chow, and J. Kornfield, 1977: A Comparative Study of the Effects of Albedo Change on Drought in Semi–Arid Regions. *Journal of the Atmospheric Sciences*, **34 (9)**, 1366–1385, doi:10.1175/1520-0469(1977)034⟨1366:ACSOTE⟩2.0.CO;2, URL http://dx.doi.org/10.1175/1520-0469(1977)034{\%}3C1366:ACSOTE{\%}3E2.0.CO;2.

Charney, J., P. H. Stone, and W. J. Quirk, 1975: Drought in the sahara: a biogeophysical feedback mechanism. *Science (New York, N.Y.)*, **187 (4175)**, 434–435, doi:10.1126/science.187.4175.434.

Charney, J. G., 1975: Dynamics of Deserts and Drought in Sahel. *Quarterly Journal of the Royal Meteorological Society*, **101 (428)**, 193–202, doi:10.1002/qj.49710142802, URL http://dx.doi.org/10.1002/qj.49710142802{\%}5Cnpapers2://publication/doi/10.1002/qj.49710142802.

Chen, G. S., M. Notaro, Z. Liu, and Y. Liu, 2012: Simulated local and remote biophysical effects of afforestation over the Southeast United States in boreal summer. *Journal of Climate*, **25 (13)**, 4511–4522, doi:10.1175/JCLI-D-11-00317.1.

Cheruy, F., J. L. Dufresne, S. Aït Mesbah, J. Y. Grandpeix, and F. Wang, 2017: Role of Soil Thermal Inertia in Surface Temperature and Soil Moisture-Temperature Feedback. *Journal of Advances in Modeling Earth Systems*, **9 (8)**, 2906–2919, doi:10.1002/2017MS001036.

Chiang, J. C., and A. R. Friedman, 2012: Extratropical Cooling, Interhemispheric Thermal Gradients, and Tropical Climate Change. *Annual Review of Earth and Planetary Sciences*, **40 (1)**, 383–412, doi:10.1146/annurev-earth-042711-105545, URL http://www.annualreviews.org/doi/10.1146/annurev-earth-042711-105545.

Chiang, J. C. H., and C. M. Bitz, 2005: Influence of high latitude ice cover on the marine Intertropical Convergence Zone. *Climate Dynamics*, **25 (5)**, 477–496, doi:10.1007/s00382-005-0040-5.

Compo, G. P., and Coauthors, 2011: The Twentieth Century Reanalysis Project. **(January)**, 1–28, doi:10.1002/qj.776.

Davin, E. L., N. de Noblet-Ducoudré, N. de Noblet-Ducoudre, N. de Noblet-Ducoudré, and N. de Noblet-Ducoudre, 2010: Climatic Impact of Global-Scale Deforestation: Radiative versus Nonradiative Processes. *Journal of Climate*, **23 (1)**, 97–112, doi:10.1175/2009JCLI3102.1, URL http://journals.ametsoc.org/doi/abs/10.1175/2009JCLI3102.1.

De Noblet-Ducoudré, N., and Coauthors, 2012: Determining robust impacts of land-use-induced land cover changes on surface climate over North America and Eurasia: Results from the first set of LUCID experiments. *Journal of Climate*, **25 (9)**, 3261–3281, doi:10.1175/JCLI-D-11-00338.1.

Devaraju, N., G. Bala, and A. Modak, 2015: Effects of large-scale deforestation on precipitation in the monsoon regions: Remote versus local effects. *Proceedings of the National Academy of Sciences*, **112 (11)**, 201423 439, doi:10.1073/pnas.1423439112, URL http://www.pnas.org/content/early/2015/02/23/1423439112http://www.pnas.org/content/early/2015/02/23/1423439112.full.pdf.

Devaraju, N., N. de Noblet-Ducoudré, B. Quesada, and G. Bala, 2018: Quantifying the relative importance of direct and indirect biophysical effects of deforestation on surface temperature and teleconnections. *Journal of Climate*, **31 (10)**, 3811–3829, doi:10.1175/JCLI-D-17-0563.1.

Dirmeyer, P. A., 2001: An Evaluation of the Strength of Land Atmosphere Coupling. *Journal of Hydrometeorology*, **2 (4)**, 329–344.

Frierson, D. M. W., and Y.-T. T. Hwang, 2012: Extratropical influence on ITCZ shifts in slab ocean simulations of global warming. *Journal of Climate*, **25 (2)**, 720–733, doi:10.1175/JCLI-D-11-00116.1.

Garcia, E. S., A. L. S. Swann, J. C. Villegas, D. D. Breshears, D. J. Law, S. R. Saleska, and S. C. Stark, 2016: Synergistic ecoclimate teleconnections from forest loss in different regions structure global ecological responses. *PLoS ONE*, **11 (11)**, 1–12, doi:10.1371/journal.pone.0165042.

Gibbard, S., K. Caldeira, G. Bala, T. J. Phillips, and M. Wickett, 2005: Climate effects of global land cover change. *Geophysical Research Letters*, **32 (23)**, L23 705, doi:10.1029/2005GL024550.

Hunke, E. C., W. H. Lipscomb, A. K. Turner, N. Jeffery, and S. Elliott, 2013: CICE : the Los Alamos Sea Ice Model Documentation and Software User ' s Manual LA-CC-06-012. 115.

Hurrell, J. W., and Coauthors, 2013: The community earth system model: A framework for collaborative research. *Bulletin of the American Meteorological Society*, **94 (9)**, 1339–1360, doi:10.1175/BAMS-D-12-00121.1.

Kang, S. M., I. M. Held, D. M. W. Frierson, and M. Zhao, 2008: The response of the ITCZ to extratropical thermal forcing: Idealized slab-ocean experiments with a GCM. *Journal of Climate*, **21 (14)**, 3521–3532, doi:10.1175/2007JCLI2146.1.

Kooperman, G. J., Y. Chen, F. M. Hoffman, C. D. Koven, K. Lindsay, M. S. Pritchard, A. L. Swann, and J. T. Randerson, 2018: Forest response to rising CO2 drives zonally asymmetric rainfall change over tropical land. *Nature Climate Change*, **8**, 434–440, doi:10.1038/s41558-018-0144-7, URL http://dx.doi.org/10.1038/s41558-018-0144-7http://www.cesm.ucar.edu/events/wg-meetings/2017/presentations/bgcwg+lmwg/kooperman.pdf.

Laguë, M. M., and A. L. S. Swann, 2016: Progressive Midlatitude Afforestation: Impacts on Clouds, Global Energy Transport, and Precipitation. *Journal of Climate*, **29 (15)**, 5561–5573, doi:10.1175/JCLI-D-15-0748.1, URL http://journals.ametsoc.org/doi/10.1175/JCLI-D-15-0748.1http://dx.doi.org/10.1175/JCLI-D-15-0748.1http://journals.ametsoc.org/doi/abs/10.1175/JCLI-D-15-0748.1?af=R.

LANS, 2017: CICE5. Tech. rep., Los Alamos National Security, LLC (LANS). URL https://cice-consortium-cice.readthedocs.io/en/cice6.0.0.alpha/cice{_}1{_}introduction.html{\#}cice-v5-0.

Lawrence, D., and Coauthors, 2018: Technical Description of version 5.0 of the Community Land Model (CLM). Tech. rep., National Center for Atmospheric Research, Boulder, Colorado.

Lee, X., and Coauthors, 2011: Observed increase in local cooling effect of deforestation at higher latitudes. *Nature*, **479 (7373)**, 384–387, doi:10.1038/nature10588, URL http://dx.doi.org/10.1038/nature10588http://files/1142/Leeetal.-2011-Observedincreaseinlocalcoolingeffectofdefor.pdf.

Manabe, S., and K. Bryan, 1969: Climate Calculations with a Combined Ocean-Atmosphere Model. URL http://journals.ametsoc.org/doi/abs/10.1175/1520-0469{\%}281969{\%}29026{\%}3C0786{\%}3ACCWACO{\%}3E2.0.CO{\%}3B2, 786–789 pp., doi: 10.1175/1520-0469(1969)026⟨0786:CCWACO⟩2.0.CO;2.

Medvigy, D., R. L. Walko, M. J. Otte, and R. Avissar, 2013: Simulated changes in Northwest U.S. Climate in response to Amazon deforestation. *Journal of Climate*, **26 (22)**, 9115–9136, doi:10.1175/JCLI-D-12-00775.1.

Milly, P. C. D., and a. B. Shmakin, 2002: Global Modeling of Land Water and Energy Balances. Part I: The Land Dynamics (LaD) Model. *Journal of Hydrometeorology*, **3 (3)**, 283–299, doi:10.1175/1525-7541(2002)003⟨0283:GMOLWA⟩2.0.CO;2, URL http://journals.ametsoc.org/doi/abs/10.1175/1525-7541{\%}282002{\%}29003{\%}3C0283{\%}3AGMOLWA{\%}3E2.0.CO{\%}3B2.

Neale, R. B., and Coauthors, 2012: Description of the NCAR community atmosphere model (CAM 5.0). *NCAR Tech. Note NCAR/TN-486+STR*.

Park, S., and C. S. Bretherton, 2009: The University of Washington Shallow Convection and Moist Turbulence Schemes and Their Impact on Climate Simulations with the Community Atmosphere Model. *Journal of Climate*, **22 (12)**, 3449–3469, doi:10.1175/2008JCLI2557.1, URL http://journals.ametsoc.org/doi/abs/10.1175/2008JCLI2557.1.

Pitman, A. J., and Coauthors, 2009: Uncertainties in climate responses to past land cover change: First results from the LUCID intercomparison study. *Geophysical Research Letters*, **36 (14)**, 1–6, doi:10.1029/2009GL039076.

Shukla, J., and Y. Mintz, 1982: Influence of land-surface evapotranspiration on the earth's climate. *Science*, **215 (4539)**, 1498–1501, doi:10.1126/science.215.4539.1498.

Sud, Y. C., J. Shukla, and Y. Mintz, 1988: Influence of Land Surface Roughness on Atmospheric Circulation and Precipitation: A Sensitivity Study with a General Circulation Model. URL http://journals.ametsoc.org/doi/abs/10.1175/1520-0450(1988)027{\%}3C1036:IOLSRO{\%}3E2.0.CO;2{\%}5Cn(null), 1036–1054 pp., doi:10.1175/1520-0450(1988)027⟨1036:IOLSRO⟩2.0.CO;2.

Swann, A. L. S., I. Y. Fung, and J. C. H. Chiang, 2012: Mid-latitude afforestation shifts general circulation and tropical precipitation. *Proceedings of the National Academy of Sciences*, **109 (3)**, 712–716, doi:10.1073/pnas.1116706108.

Swann, A. L. S., I. Y. Fung, S. Levis, G. B. Bonan, and S. C. Doney, 2010: Changes in Arctic vegetation amplify high-latitude warming through the greenhouse effect. *Proceedings of the National Academy of Sciences*, **107 (4)**, 1295–1300, doi:10.1073/pnas.0913846107, URL http://www.pnas.org/cgi/doi/10.1073/pnas.0913846107.

Swann, A. L. S., and Coauthors, 2018: Continental-scale consequences of tree die-offs in North America: Identifying where forest loss matters most. *Environmental Research Letters*, **13 (5)**, 55 014, doi:10.1088/1748-9326/aaba0f.

Vargas Zeppetello, L. R., A. Donohoe, and D. S. Battisti, 2019: Does Surface Temperature Respond to or Determine Downwelling Longwave Radiation? *Geophysical Research Letters*, **46**, 2781–2789, doi:10.1029/2019GL082220.

Zhang, X., S. Chen, M. Liu, D. Pei, and H. Sun, 2005: Improved Water Use Efficiency Associated with Cultivars and Agronomic Management in the North China Plain Xiying. *Agronomy*

Journal, **97 (3)**, 783–790, doi:10.2134/agronj2004.0194.

LIST OF TABLES

		Experiments:								
		Perturbation Variable								
		albedo			evap. res			vegetation height		
Surface Value	α (unitless)	**0.1**	**0.2**	**0.3**	0.2	0.2	0.2	0.2	0.2	0.2
	r_s (s/m)	100	100	100	**30**	**100**	**200**	100	100	100
	h_c (m)	0.1	0.1	0.1	0.1	0.1	0.1	**0.1**	**1.0**	**2.0**

TABLE 1. The values for each experiment are given, with each column of three values corresponding to a single experiment. Values for albedo α are given in the top row, evaporative resistance r_s (s/m) in the middle row, and vegetation height h_c (m) in the bottom row. Columns are grouped into the variable being perturbed; note that the 'baseline' simulation of $\alpha = 0.2$, $r_s = 100$, $h_c = 0.1$ appears three times but is actually a single simulation.

LIST OF FIGURES

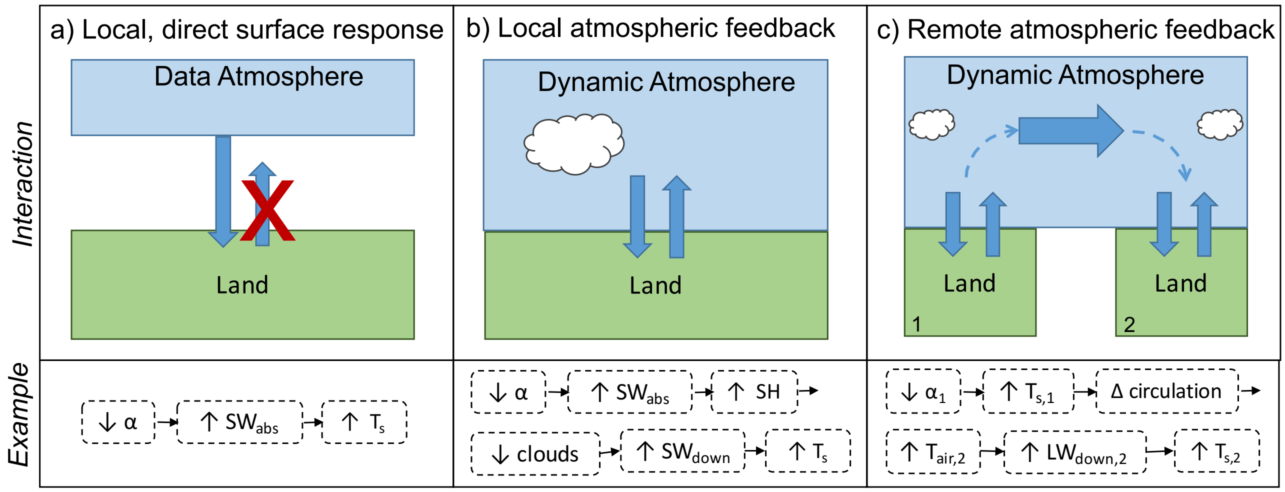

FIG. 1. Three types of land atmosphere interactions: (a) the direct, local response of the surface to the atmosphere (with no feedbacks); (b) local atmospheric feedbacks, where changes in the atmosphere above a modified land surface occur because of the modified land surface below that atmospheric column; (c) remote atmospheric feedbacks, where a change in land at location 1 drives a large-scale atmospheric response which can in turn impact the land at location 2. Examples of each feedback consider the impact of a change in albedo α on absorbed shortwave energy SW_{abs}, sensible heat flux SH, cloud cover, downwards shortwave energy at the surface SW_{down}, downwards longwave energy at the surface LW_{down}, and surface temperature T_s.

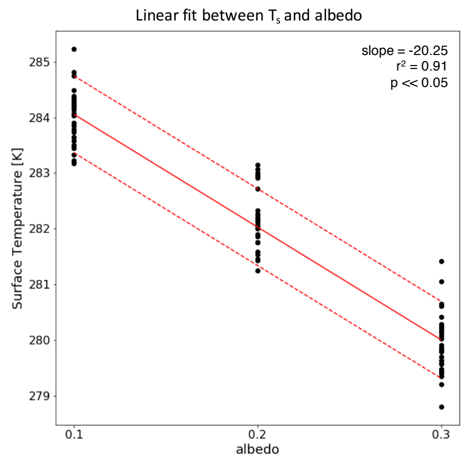

FIG. 2. Example of calculation of the slope $\frac{\partial \mathrm{atm}}{\partial \mathrm{lnd}}$ for the response of surface (skin) temperature to changing surface albedo at 102.5°W, 42°N. Individual black dots show the annual mean temperature for a single year (30 years per spun-up simulation) at each of the three albedo levels. The solid red line shows the slope of the response, while the dashed red lines show 1 standard error around the slope. Because this example has a strong response, the p value, which we use to test if the slope is different from zero, is very small (p$\approx 10^{-47}$).

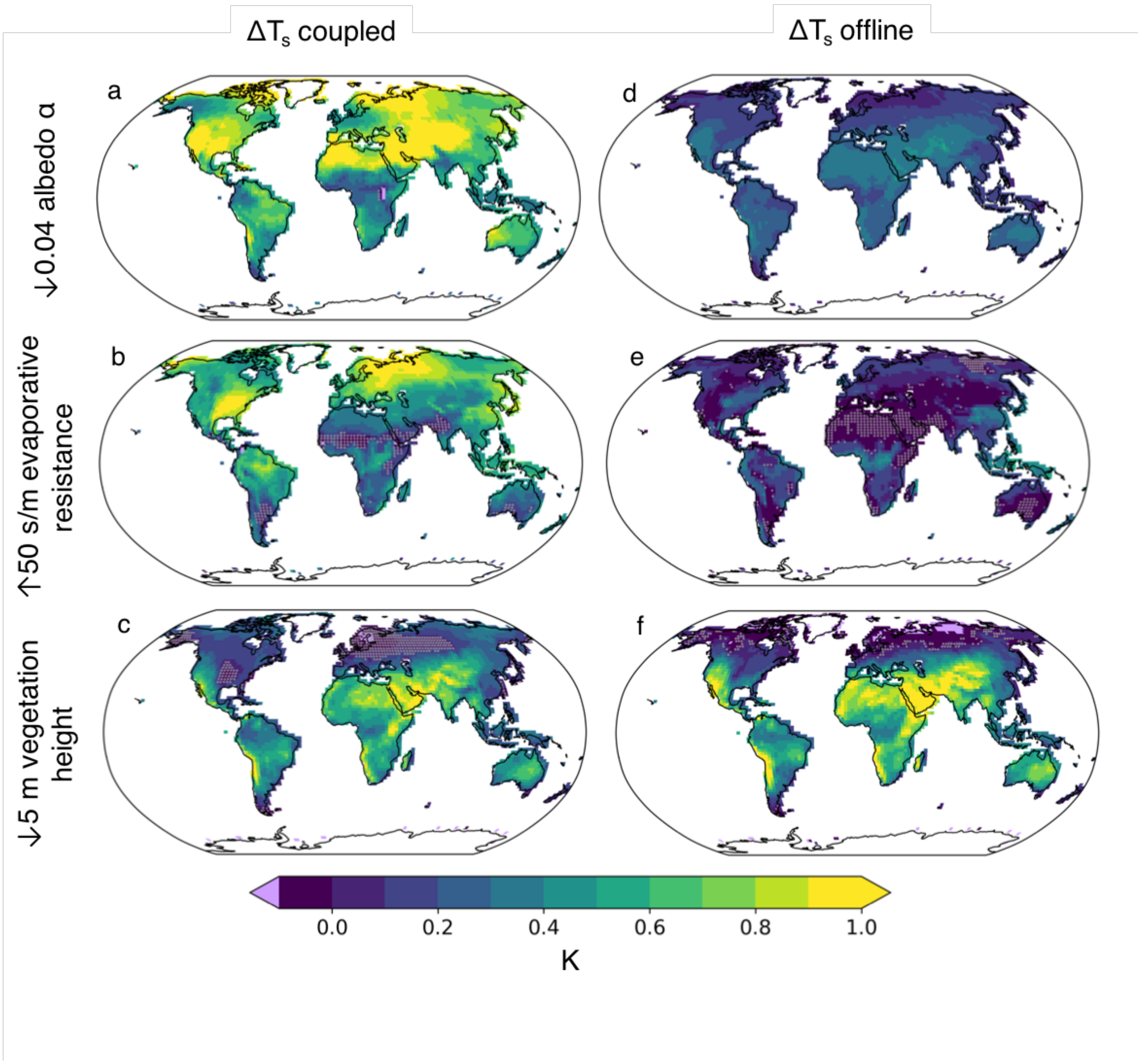

FIG. 3. Annual mean scaled surface temperature T_s response [K] for (a-c) coupled simulations and (d-f) offline simulations, per 0.04 darkening of the surface albedo (a,d), 50 s/m increase in evaporative resistance (b,e), and 5.0 m decrease in vegetation height (c,f). Violet regions ($\Delta T_s < 0.1$) indicate regions where the temperature cooled substantially in response to the prescribed surface change. Stippling indicates regions where the slope is not significantly different from zero ($p > 0.05$).

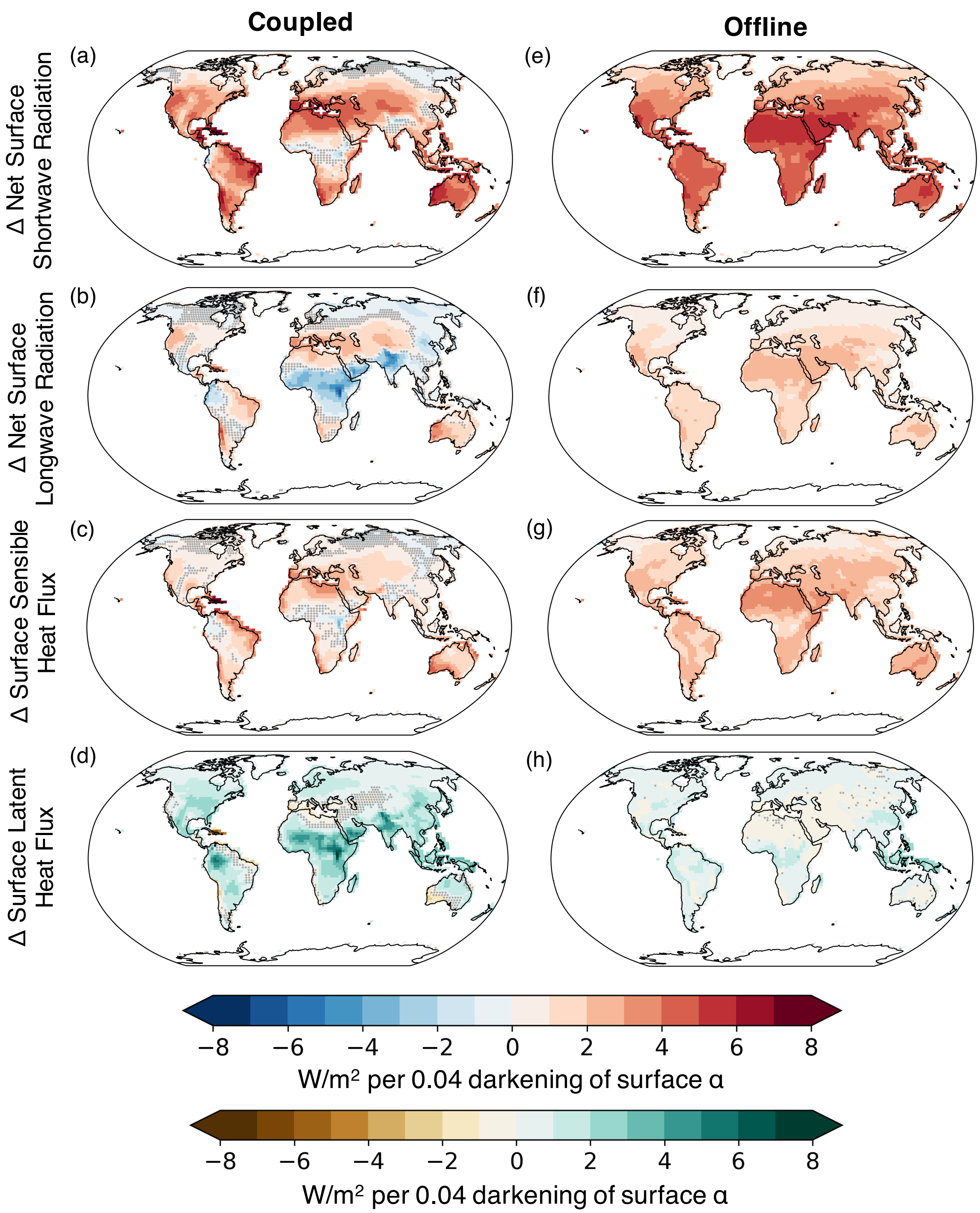

956 FIG. 4. Annual mean change in surface energy fluxes [W/m^2] per 0.04 decrease in global land albedo. Fluxes
957 from the coupled simulations (a-d) are shown on the left, while offline fluxes (e-h) are shown on the right.
958 Fluxes shown are net shortwave radiation (a,e), net longwave radiation (b,f), sensible heat flux (c,g), and latent
959 heat flux (d,h). Red (blue) indicates an increase (decrease) in net shortwave radiation, net longwave radiation,
960 and sensible heat flux. Green (brown) indicates an increase (decrease) in latent heat flux. Stippling indicates
961 regions where the response is not significant ($p > 0.05$).

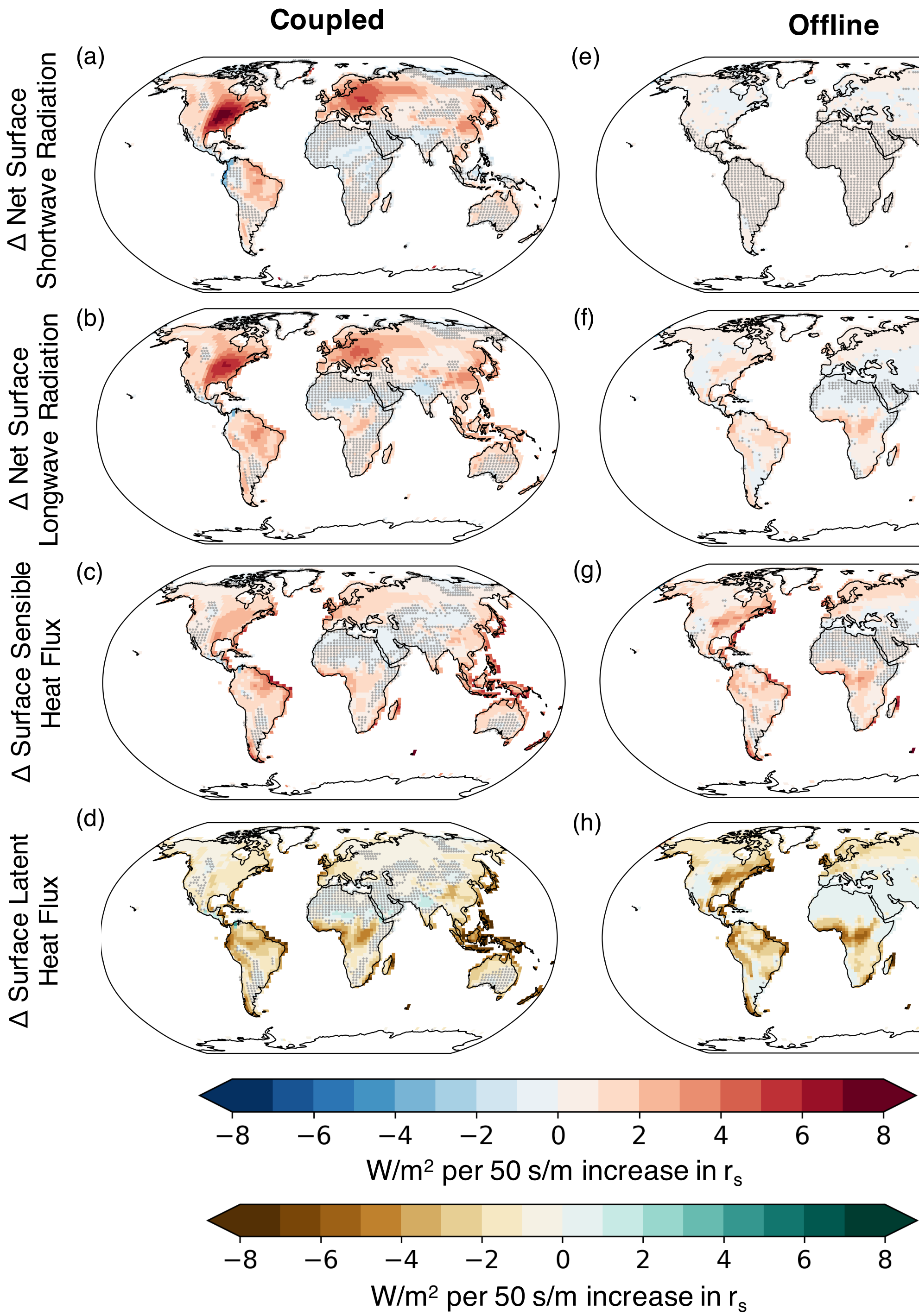

FIG. 5. Annual mean change in surface energy fluxes [W/m^2] per 50 s/m increase in evaporative resistance. Fluxes from the coupled simulations (a-d) are shown on the left, while offline fluxes (e-h) are shown on the right. Fluxes shown are net shortwave radiation (a,e), net longwave radiation (b,f), sensible heat flux (c,g), and latent heat flux (d,h). Red (blue) indicates an increase (decrease) in net shortwave radiation, net longwave radiation, and sensible heat flux. Green (brown) indicates an increase (decrease) in latent heat flux. Stippling indicates regions where the response is not significant ($p > 0.05$).

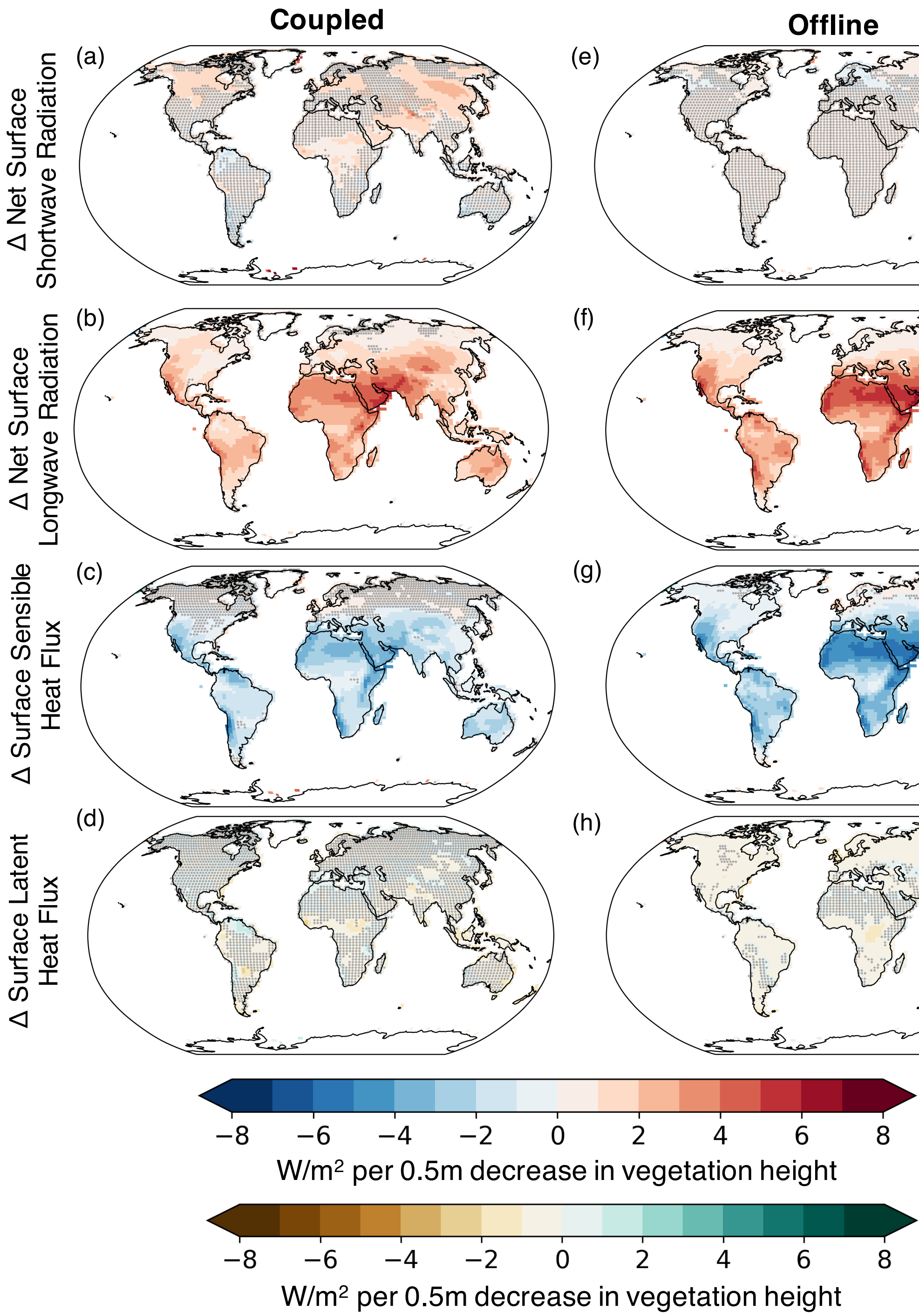

FIG. 6. Annual mean change in surface energy fluxes [W/m^2] per 0.5 m decrease in vegetation height. Fluxes from the coupled simulations (a-d) are shown on the left, while offline fluxes (e-h) are shown on the right. Fluxes shown are net shortwave radiation (a,e), net longwave radiation (b,f), sensible heat flux (c,g), and latent heat flux (d,h). Red (blue) indicates an increase (decrease) in net shortwave radiation, net longwave radiation, and sensible heat flux. Green (brown) indicates an increase (decrease) in latent heat flux. Stippling indicates regions where the response is not significant ($p > 0.05$).

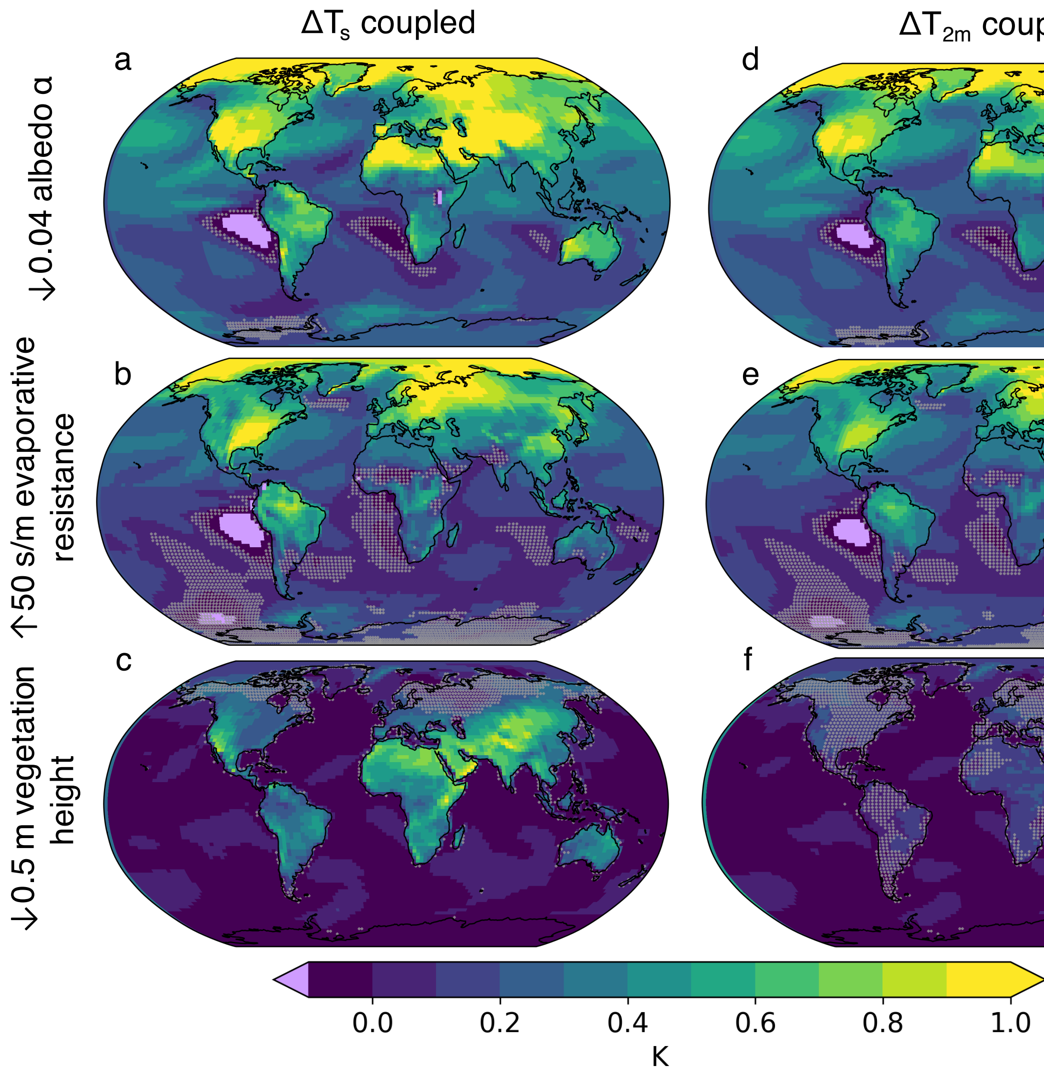

974 FIG. 7. Change in surface temperature (left) and 2m air temperature (right) [K] per 0.04 decrease in land
975 surface albedo (a,d), 50 s/m increase in land surface evaporative resistance (b,e), and 0.5m decrease in land
976 surface vegetation height . Stippling indicates regions which are not significant ($p < 0.05$), while violet shows
977 areas where the temperature response is less than -0.1 K.

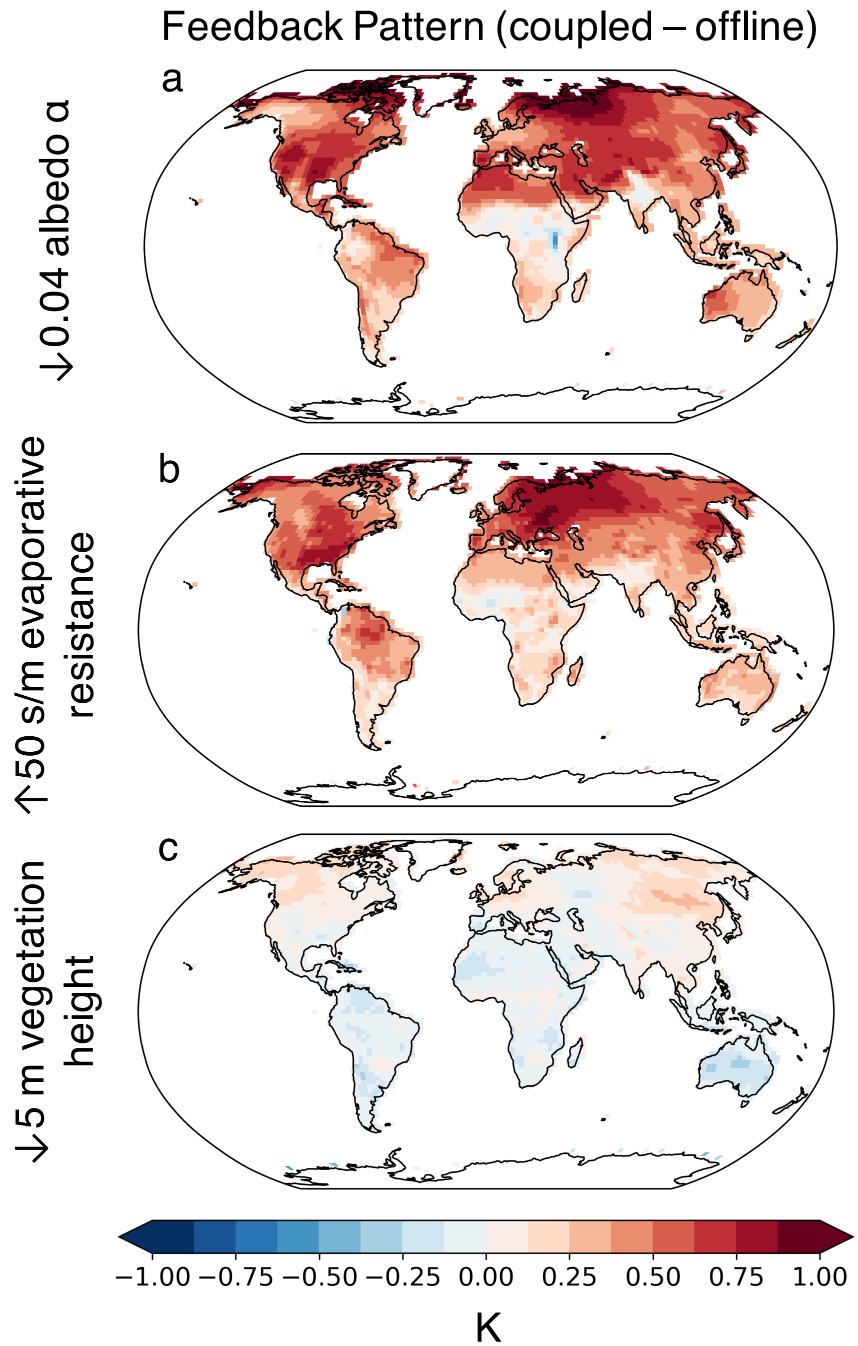

978 FIG. 8. Difference in surface temperature response in coupled - offline simulations for (a) albedo, (b) evapo-
979 rative resistance, and (c) vegetation height.

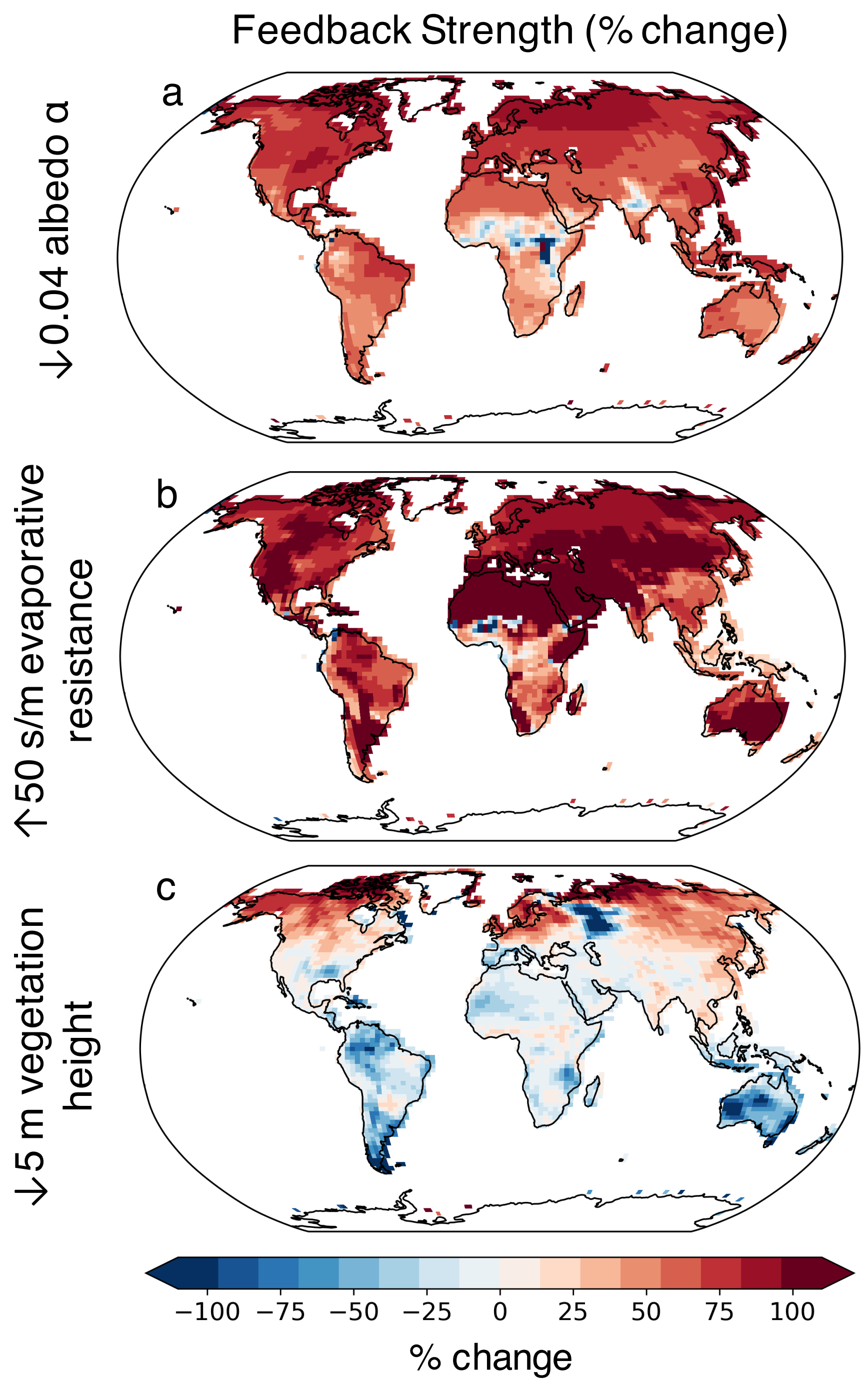

980 FIG. 9. Atmospheric feedback strength (percent change) for (a) albedo, (b) evaporative resistance, and (c)
981 vegetation height.

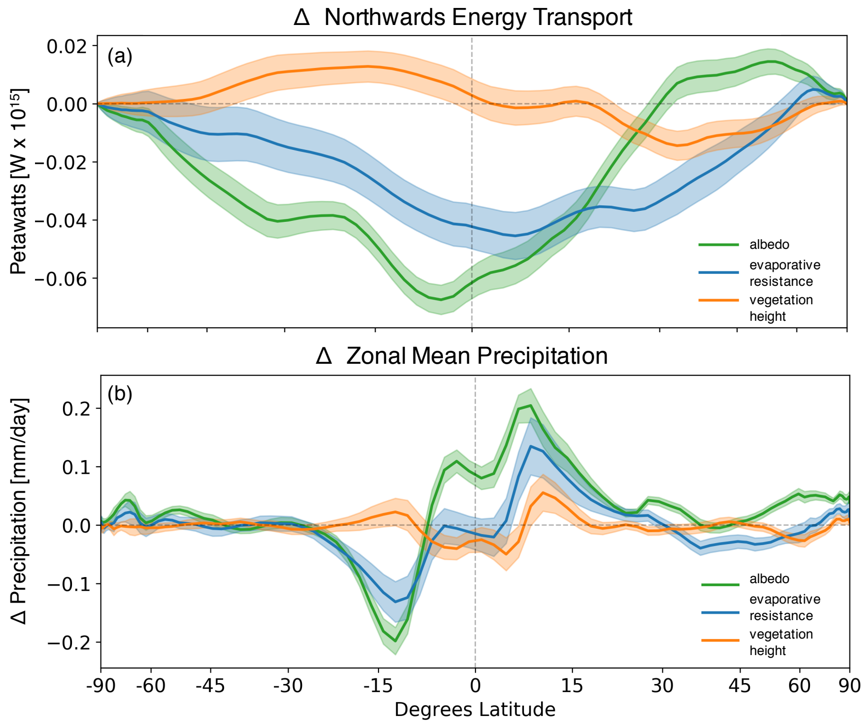

FIG. 10. Change in (a) northward energy transport [Petawatts] and (b) zonal mean precipitation [mm/day] per 0.04 decrease in albedo (green), 50 s/m increase in evaporative resistance (blue), and 0.5 m decrease in vegetation height (orange). Solid lines show the annual mean change in each field per change in each surface property. Shading indicates 1 standard deviation around that mean change. Northwards energy transport F_ϕ at each latitude ϕ is calculated as $F_\phi = \int_{-\pi/2}^{\phi} \int_0^{2\pi} R_{TOA} a^2 \cos\phi \, d\lambda \, d\phi$, where a is the radius of the Earth, R_{TOA} is the net radiation at the top of the atmosphere, ϕ is latitude, and λ is longitude.

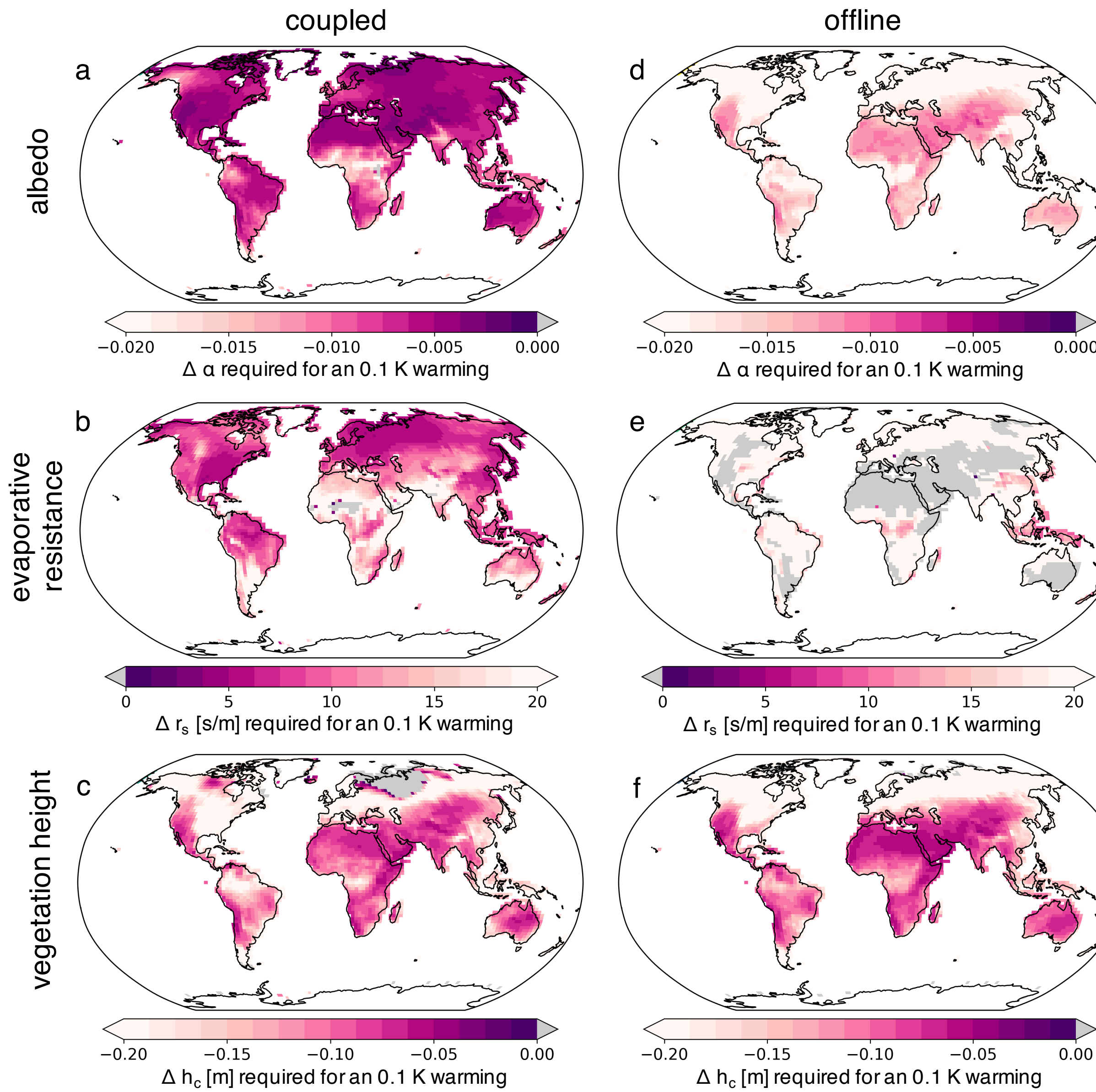

988 FIG. 11. Change in surface property required to drive an 0.1 K warming in the coupled (left) and offline
989 (right) model simulations, for albedo (top), evaporative resistance (middle), and vegetation height (bottom).
990 Note that negative numbers for albedo (darker colors) mean a decrease in albedo; positive numbers for evap-
991 orative resistance mean an increase in resistance; negative numbers for vegetation height mean a reduction in
992 vegetation height (smoother surface). Greyed areas show regions where decreased albedo, increased resistance,
993 and decreased vegetation height cool (typically regions which are not significant in figure 3).

Supplemental Material for "Separating the impact of individual land surface properties on the terrestrial surface energy budget in both the coupled and un-coupled land-atmosphere system"

Marysa Laguë, Abigail L. S. Swann, Gordon B. Bonan

June 11, 2019

---

1 Simple Land Interface Model (SLIM) Model Description

1.1 Introduction

The Simple Land Interface Model (SLIM) is a simple land model written to couple with a global Earth System Model (ESM). In particular, this model is currently written to couple to the Community Earth System Model (CESM [Hurrell et al., 2013]) in place of the Community Land Model (CLM [Lawrence et al., 2018]).

This simple model bears strong resemblance to some of the early global land surface models, and draws heavily from the parameterizations set forth in models including the land surface model of Manabe [1969]; the Biosphere Atmosphere Transfer Scheme (BATS) [Dickinson et al., 1993]; the Land Surface Model version 1 (LSM 1.0) [Bonan, 1996]; and the Land Dynamics Model (LaD) [Milly and Shmakin, 2002a], which was used as the LM2 land surface model in the GFDL AM2LM2 model [Anderson et al., 2004].

1.2 Land Surface Model

The simple land model solves a linearized bulk surface energy budget coupled with soil temperatures and bucket hydrology. Various physical properties determine how energy is partitioned within the surface energy budget (see table 1). Hydrology is represented with a simple "bucket", which has a prescribed capacity. Additionally, there is a simple snow model which allows for land-albedo feedbacks during winter months.

1.2.1 Land Surface Properties

The land model has several properties which are defined by the user for each land point. These variables are listed in table 1. The variables are provided to the model using a netcdf file provided by the user, where each value is specified for every terrestrial gridpoint.

The surface albedo determines how much incoming shortwave radiation is reflected from the land surface. The atmospheric model passes four different 'streams' of radiation to the land model: both a direct and diffuse value for visible light (0.2-0.7 μm) and near-infrared light (0.7 - 12.0 μm).

Albedos for each of these radiative streams are prescribed both for bare ground and snow-covered ground. The emissivity ε of the ground can be specified. Land surface emissivities range from 0.9 to 1.0 [Bonan, 2002]; if unspecified, and for the purposes of this study, it is assumed that $\varepsilon = 1$ over all land areas.

In order to calculate temperature profiles within the 10 soil layers, the soil thermal conductivity κ and heat capacity c_v must be specified. Over glaciated regions (specified using a user-defined glacier mask), the thermal resistance and heat capacity of ice rather than soil are used. The bucket model for hydrology requires a bucket capacity W_{max} (the maximum amount of water each gridcell can hold) and a surface "lid" resistance to evaporation r_s. The aerodynamic roughness is calculated from the vegetation height h_c. A simple snow model is included in SLIM; as snow accumulates on the land surface, it begins to mask the albedo of the snow-free surface such that the surface albedo approaches that of snow.

1.2.2 Atmospheric Fluxes

At each time step the land model is run, information is required about the state of the atmosphere. This information can come either from a data atmosphere model (e.g. reanalysis), or from a coupled atmospheric model such as the Community Atmosphere Model [Neale et al., 2012]. The variables required from the atmosphere by the land model are given in table 2.

1.2.3 Surface Energy Budget

This model solves a linearized surface energy budget (eq 1) to calculate fluxes of energy and water to the atmosphere at each time step, and to calculate the surface temperature, temperature profile of the soil column, snow depth, and available water in each gridcell.

$$SW^{\downarrow} + LW^{\downarrow} = SW^{\uparrow} + LW^{\uparrow} + LH + SH + G \quad (1)$$

From the atmosphere, the land model receives the amount of downwards solar radiation $SW^{\downarrow}$ for four radiation streams (visible direct, visible diffuse, near-infrared direct, and near-infrared diffuse), the amount of downwards longwave radiation $LW^{\downarrow}$, and information about the temperature, humidity, and wind speed of the bottom of the atmosphere. The land model calculates the reflected shortwave radiation $SW^{\uparrow}$, the upwards longwave radiation $LW^{\uparrow}$, the sensible heat flux SH, latent heat flux LH, and ground heat uptake G.

Equation 1 can be rewritten as

$$\begin{aligned} (1-\alpha)SW^{\downarrow} + \varepsilon LW^{\downarrow} - LW^{\uparrow} &= LH + SH + G \\ R_{in} &= LW^{\uparrow} + LH + SH + G \\ R_{net} &= LH + SH + G \end{aligned} \tag{2}$$

where α is the albedo of the surface. $LW^{\uparrow} = \varepsilon\sigma T_s^4$ is the longwave radiation emitted by the surface, which is a function of surface temperature T_s and surface emissitivty ε. R_{in} is the total absorbed radiative energy at the surface ($SW_{abs} + LW_{abs}$). R_{net} is the net radiative energy coming into the surface, which must be balanced by the turbulent energy fluxes (latent and sensible heat) and heat uptake by the land (soil or snow).

R_{in} can be directly calculated from the surface properties and atmospheric fluxes; $LW^{\uparrow} = \varepsilon\sigma T_s^4$, LH, SH, and G must each be found by evaluating the land model at each time step. In order to numerically calculate the balance of these fluxes at each time step, equation 2 is linearized around the change in surface temperature T_s.

That is, we calculate a ‘first guess’ at a flux (using the surface temperature from the previous time step), as well as the derivative of that flux with respect to surface temperature. We proceed to calculate a new surface temperature for the current time step, then update the surface fluxes given the initial estimate and its derivative with respect to temperature. This is equivalent to taking a first order Taylor expansion of each surface flux (equation 4), where some flux F at time $i+1$ is approximated by its value at time i and its derivative with respect to surface temperature T_s.

$$F(T_s^{i+1}) = F(T_s^i) + \frac{\delta F(T_s^i)}{\delta T_s}(T_s^{i+1} - T_i) + \mathcal{O}(T^2) \tag{3}$$

$$F(T_s^{i+1}) \approx F(T_s^i) + \frac{\delta F(T_s^i)}{\delta T_s}(T_s^{i+1} - T_s^i) \tag{4}$$

We solve the surface energy budget by linearizing each term with a first-order Taylor Expansion with derivatives w.r.t. surface temperature. i.e. for some surface flux S, its value at the $i+1$ time step is its value at the ith time step plus its derivative w.r.t. temperature times the change in surface temperature:

$$S^{i+1} = S^i + \frac{\partial S}{\partial T_s}\Delta T_s. \tag{5}$$

For our longwave radiation, sensible heat flux, latent heat flux, and soil heat flux, this gives:

$$LW^{\uparrow i+1} = LW^{\uparrow i} + \frac{\partial LW^{\uparrow}}{\partial T_s}\Delta T_s \tag{6}$$

$$SH^{i+1} = SH^i + \frac{\partial SH}{\partial T_s}\Delta T_s \tag{7}$$

$$LH^{i+1} = LH^i + \frac{\partial LH}{\partial T_s}\Delta T_s \tag{8}$$

$$G^{i+1} = G^i + \frac{\partial G}{\partial T_s}\Delta T_s \tag{9}$$

$$R_{in}^{i+1} = (1-\alpha)SW^{\downarrow i+1} - \varepsilon LW^{\downarrow i+1} \tag{10}$$

$$\tag{11}$$

Thus, in order to calculate the surface fluxes for the $i+1$ time step, we must first calculate the change in surface temperature ΔT_s, and the derivative of each flux with respect to temperature.

1.3 Radiative Fluxes

The longwave radiation $LW^{\uparrow}$ [W/m^2] emitted from the surface, and its temperature derivative, are given by equations 12-13 as a function of the surface temperature at the preceding timestep T_s^i, where ε is the emissivity of the surface, and $\sigma = 5.670373 \times 10^{-8}$ W/m^2/K^4 is the Stefan-

Boltzmann constant.

$$LW^{\uparrow} = \varepsilon\sigma(T_s^i)^4 \tag{12}$$

$$\frac{\delta LW^{\uparrow}}{\delta T_s} = 4\varepsilon\sigma(T_s^i)^3 \tag{13}$$

The absorbed downwards longwave radiation is a direct function of the downwelling longwave radiation $LW^{\downarrow}$ and the surface emmisivity ε. The absorbed shortwave radiation is a function of the downwelling shortwave radiation $SW^{\downarrow}$ in each of the four radiation streams, and the surface albedo for each corresponding radiative stream.

Bare-ground albedo is prescribed at each gridcell by the user. When a gridcell is free of snow, the bare-ground albedos are used. When there is snow on the ground (S, [kg/m^2]), a blend of the bare-ground and snow-covered albedos are used, following equation 14 (this is the default implementation of snow-covered ground albedo in Anderson et al. [2004], Milly and Shmakin [2002b]). A snow-masking factor M_s [kg] is used to define how steeply the bare-ground albedo should approach the snow-covered ground albedo (figure 1). A typical value of M_s used in SLIM is 50 kg/m^2, which corresponds to roughly 25cm of snow (assuming a snow density of 200 kg/m^3, typical of settled snow [Paterson, 1994]),

$$\alpha_j = \begin{cases} \alpha_{soil,j} & \mathrm{S} = 0 \\ (1 - \frac{S}{S+M_s})\alpha_{soil,j} + \frac{S}{S+M_s}\alpha_{snow,j} & 0 < \mathrm{S} < M_s \\ \alpha_{snow,j} & \mathrm{S} > M_s. \end{cases} \tag{14}$$

So, the total amount of incoming radiative energy from the atmosphere at each time step can be directly calculated as

$$R_{in}^{i+1} = \sum_j (1 - \alpha_j) SW_j^{\downarrow i+1} + \varepsilon LW^{\downarrow i+1} \tag{15}$$

for the four shortwave radiative streams j.

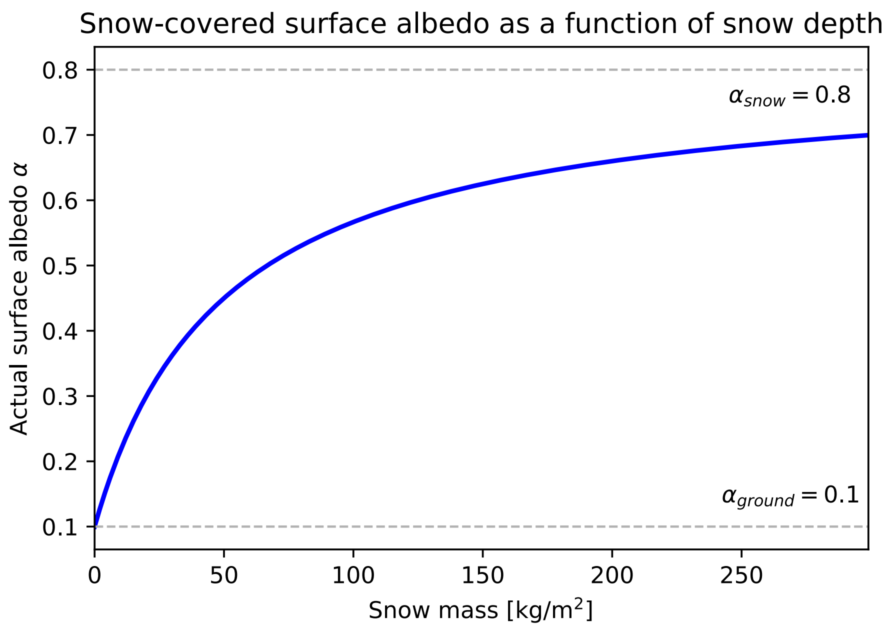

Figure 1: The albedo of a snow-covered gridcell as function of snow mass.

111 1.4 Turbulent Heat Fluxes

The calculation of the turbulent heat fluxes (sensible and latent heat) relies on Monin-Obukhov theory [Monin and Obukhov, 1954]. Using the temperature, humidity, and wind speed of the bottom of the atmosphere, along with the temperature and humidity at the surface, the flux of heat and water can be calculated. These fluxes are influenced by the roughness of the land surface. The vegetation height h_c [m] provided by the surface property netcdf file is used to calculate a displacement height d (equation 16), a roughness length for momentum z_{0m} (equation 17), and a roughness length for heat z_{0h} (equation 18).

$$d = 0.7h_c \tag{16}$$

$$z_{0m} = 0.1h_c \tag{17}$$

$$z_{0h} = 0.1z_{0m} \tag{18}$$

The above roughness lengths are used to calculate an Obukhov Length L, which in turn is used with the atmospheric temperature, humidity, and wind speed at the lowest atmospheric level to calculate an aerodynamic resistance for momentum r_{am}, heat r_{ah}, and moisture r_{aw} (in [s/m]). The Obukhov Length is calculated iteratively, with an initial estimate L_0 used to calculate the next estimate L_1. In order to calculate the Obukhov Length, two intermediate fuctions ψ_m (for momentum) and ψ_h (for heat) are required (equations 20-21).

$$y = (1 - 16x)^{0.25} \tag{19}$$

$$\psi_m(x) = \begin{cases} 2\log(\frac{1+y}{2}) + \log(\frac{1+y^2}{2}) - 2\arctan(y) + \frac{\pi}{2} & \text{if} \quad x < 0 \\ -5x & \text{if} \quad x \geq 0 \end{cases} \tag{20}$$

$$\psi_h(x) = \begin{cases} 2\log(\frac{1+y^2}{2}) & \text{if} \quad x < 0 \\ -5x & \text{if} \quad x \geq 0 \end{cases} \tag{21}$$

We use the reference level (typically 10m) atmospheric winds u_{ref}, temperature t_{ref}, and water vapour q_{ref}, the surface temperature t_s and water vapour q_s, as well as the dimensionless von Kármán constant $\kappa = 0.4$. Surface winds are assumed to be zero.

$$u^* = \frac{u_{ref}\kappa}{\log(\frac{z_{ref}-d}{z_0m}) - \psi_m(\frac{z_{ref}-d}{L_0}) + \psi_m(\frac{z_{0m}}{L_0})} \tag{22}$$

$$t^* = \frac{(t_{ref} - t_s)\kappa}{\log(\frac{z_{ref}-d}{z_0h}) - \psi_h(\frac{z_{ref}-d}{L_0}) + \psi_h(\frac{z_{0h}}{L_0})} \tag{23}$$

$$q^* = \frac{(q_{ref} - q_s)\kappa}{\log(\frac{z_{ref}-d}{z_0h}) - \psi_h(\frac{z_{ref}-d}{L_0}) + \psi_h(\frac{z_{0h}}{L_0})} \tag{24}$$

$$t_v^* = t^* + 0.61t_s q^* \tag{25}$$

$$\theta_v = \theta_{ref}(1 + 0.61q_{ref}) \tag{26}$$

Equations 22-26 are then used to make a new estimate of the Obukhov length,

$$L_1 = \frac{u^{*2}\theta_v}{\kappa g t_v^*}. \tag{27}$$

Additionally, we limit the Obukhov Length to keep it within a range that gives reasonable flux values, in the following manner; this capping is common in land models [Anderson et al., 2004, Lawrence et al., 2018].

$$\zeta_0 = \frac{z_{ref} - d}{L_1} \tag{28}$$

$$\zeta = \begin{cases} \min(2, \zeta_0) & \text{if} \quad \zeta_0 \geq 0 \\ \max(-2, \zeta_0) & \text{if} \quad \zeta_0 < 0 \end{cases} \tag{29}$$

$$L_1 = \frac{z_{ref} - d}{\zeta} \tag{30}$$

The above equations are iterated over until the difference between L_0 and L_1 is small, up to a maximum of 40 iterations per time step. If the above fails to converge in 40 iterations, the value of L_1 with the smallest difference from its corresponding L_0 is used.

Using the final value of L_1, final values of u^* and t^* are obtained, which are used to calculate the aerodynamic resistance of momentum r_{am} and heat r_{ah} (in units of [s/m]). We also calculate the aerodynamic resistance for moisture (r_{aw}), by combining the evaporative resistance for heat with the prescribed evaporative resistance r_s that the user directly controls (comparable to a bulk stomatal resistance for a canopy - this is how the user directly controls how difficult it is to evaporate water out of the bucket). The aerodynamic resistances require the use of several variables from the atmospheric reference height z_{ref} (such as wind speed and air temperature):

$$r_{am} = \frac{u_{ref}}{u^* u^*} \tag{31}$$

$$r_{ah} = \frac{\theta_{ref} - T_s}{u^* T^*} \tag{32}$$

$$r_{aw} = r_s + r_{ah}. \tag{33}$$

The sensible heat flux SH [W/m^2] is a function of the difference between the surface temperature T_s^i and the potential air temperature at the reference height θ_{ref}^i, as well as the roughness length for heat:

$$SH = c_{p,air}(T_s^i - \theta_{ref}^i)\frac{\rho_{air}}{r_{ah}} \tag{34}$$

$$\frac{\delta SH}{\delta T_s} = c_{p,air}\frac{\rho_{air}}{r_{ah}} \tag{35}$$

(where $c_{p,air}$ is the heat capacity of air and ρ_{air} is the density of air).

The latent heat flux LH [W/m^2] is a function of the difference between the surface humidity and the humidity in the atmosphere. It is further impacted by the evaporative resistance r_s, the aerodynamic resistance r_{ah}, and another term, β, which accounts for bucket fullness (equation 36).

$$\beta = \min\left(\frac{water}{0.75 \times W_{max}}, 1.0\right) \tag{36}$$

β is used to increase evaporative resistance under dry soil conditions. When the bucket is more than 75% full (ie the soil is moist), $\beta = 1$ (no additional resistance). When the bucket is less than 75% full, β decreases linearly from 1 to 0; the smaller the β term, the larger the resistance to evaporation.

The effective resistance of the land is a combination of the prescribed "lid" resistance r_s, the aerodynamic resistance due to the surface roughness r_{ah} (see equation 33), and the β value associated with how dry the soil is.

$$LH = \rho_{air}\lambda(q_s^i - q_{ref}^i)\frac{\beta}{r_{aw}} \tag{37}$$

$$\frac{\delta LH}{\delta T_s} = \rho_{air}\lambda\frac{\delta q_s}{\delta T_s}\frac{\beta}{r_{aw}} \tag{38}$$

In equation 38, ρ_{air} is the density of air, λ is the latent heat of vaporization (or sublimation, if temperatures are below freezing), q_s is the surface humidity, q_{ref} is the atmospheric humidity at some reference height, and T_s is the surface temperature. q_s, q_{ref}, and T_s are taken from the preceding time step i. Note that if the latent heat flux term attempts to evaporate (or sublimate) more water than is available in the combined water and snow buckets, the latent heat flux term is set to the total water plus snow available, and $\frac{\delta LH}{\delta T_s} = 0$, and the excess energy that would have been used by LH if more water were available is instead partitioned to SH.

1.4.1 Ground Heat Flux

The change in heat uptake by the soil $\frac{\delta G}{\delta T_s}$ requires solving the full temperature profile of the soil column. It is calculated using the energy imbalance of the other surface fluxes:

$$\begin{aligned}\frac{dG}{dT_s} &= \frac{\partial}{\partial T_s}\big(R_{in} - (LW^{\uparrow} + LH + SH)\big)\\ &= -\frac{\partial}{\partial T_s}LW^{\uparrow} - \frac{\partial}{\partial T_s}LH - \frac{\partial}{\partial T_s}SH,\end{aligned} \tag{39}$$

Heat transfer through the soil column is then calculated to get a new temperature for each soil layer, and a new surface temperature (section 1.4.3). Once the change in soil temperature at each soil layer (and specifically, the change in surface temperature T_s) is found, the total soil heat uptake G is given by

$$G^{i+1} = G^i + \frac{dG}{dT_s}(T_s^{i+1} - T_s^i), \tag{40}$$

where G^i is the energy flux into the soil at the previous time step i, $\frac{dG}{dT_s}$ is the derivative of the energy flux into the soil with respect to temperature Here, G includes both the energy used to warm/cool the soil as well as any energy used to melt snow ($G = G_{soil} + G_{snow}$).

1.4.2 Hydrology

Water enters the land system by falling from the atmosphere as snow or rain. Water can fill up the bucket in each gridcell up to the bucket capacity W_{max}; if the amount of water in a gridcell exceeds W_{max}, the excess is moved into runoff. At present, the runoff is discarded; if this model were run coupled to a dynamic ocean model, runoff water should be routed through an appropriate river-runoff scheme and added to the ocean model. Water is removed from the bucket either through runoff or evaporation (latent heat flux). A baseline value of $W_{max} = 200$kg/m^2 is used, but can be modified spatially by the user. We use 200 kg/m^2 as it falls within the range of soil water capacities (assuming a 1m deep 'bucket') in the LM2 model, which range from 63 kg/m^2 for coarse soil to 445 kg/m^2 for peat.

Snow can also fall onto grid cells. There is no limit on the amount of snow which can be held on a gridcell (note - this means snow accumulates indefinitely over the ice caps - a glacier calving scheme would need to be implemented to counteract this effect if it was undesirable for some application). The heat flux into the land G can be used to melt snow; melted snow flows into the water bucket.

The hydrology is a single layer 'bucket' with a prescribed capacity to hold water, and is not dependent on any specific soil properties. If the user wants this capacity to vary with geographically distinct soil types, they would need to feed the model a spatially varying map of maximum water content.

1.4.3 Soil Temperatures

In order to solve equation 2, we must find ΔT_s. That is, we must calculate the new surface temperature. There are 10 soil layers in this model, with the midpoints of each soil layer given by equation 41:

$$z_i = -0.025 * (\exp(0.5 * (i - 0.5)) - 1.0) \quad i \in 1, 10. \tag{41}$$

The maximum soil depth is roughly 3.5m.

Soil temperatures are calculated using a simple heat diffusion equation through the soil layers, with a zero-flux bottom boundary condition (no energy can go in or out of the soil column through the bottom) and an upper boundary condition given by the G_{soil} term in the surface energy budget equation. Since the water in the bucket hydrology model is effectively isolated from the soil column, the amount of water in a given gridcell doesn't influence the soil thermal properties. Thus, in addition to the prescribed heat capacity and thermal conductivity of the soil, there is a fixed density of freezable water in each soil layer, which is not coupled to the amount of water actually present and available for evaporation in that gridcell. The soil *does* have a fixed density of freezable water in each layer (set by default to 300 kg/m^3). That is, the thin layers near the surface have a small amount of water in the soil layer which can be frozen/thawed using heat in that soil layer, while the deeper soil layers have a larger total volume of water available to freeze/thaw. This water is always present, and interacts with the soil **only** in a thermal manner. The water in the soil layers does not interact with the hydrology portion of the model - that is, it is not moved up and down between soil layers, and cannot be evaporated. The primary reason to include this freezable water in each soil layer is to allow the model to have a more realistic timescale of soil temperature change during spring and fall at high latitudes, where it takes time for the ground to freeze and thaw. This is comparable to the representation of water and soil in the LM2 model [Anderson et al., 2004].

We use the surface energy fluxes to update the soil temperature at each layer $n = 1 : N$ in the soil column, using the equation for heat diffusion:

$$c_{v,n} \frac{\partial T}{\partial t} = -\frac{\partial F}{\partial z}, \tag{42}$$

which can be re-arranged as

$$\partial T = -\frac{\Delta t}{c_{v,n} \Delta z_n} (F_{in} - F_{out}). \tag{43}$$

In eq 43, T is the temperature $[K]$, Δt is the time step $[s]$, $c_{v,n}$ is the heat capacity of the n^{th} layer $[J/m^3/K]$, Δz_n is the thickness of soil layer n [m], and F_{in} and F_{out} are, respectively, the fluxes of energy into the top of and out of the bottom of the n^{th} soil layer $[W/m^2]$.

At each soil layer, the fluxes into and out of each soil layer are given by:

$$F_n = \begin{cases} R_{in} - (LW^{\uparrow} + LH + SH) & n = 0 \text{ (top)} \\ -\kappa_{x,n} \frac{(T_n - T_{n+1})}{(z_n - z_{n+1})} & n = 1 : (N-1) \\ 0 & n = N \text{ (zero-flux bottom).} \end{cases} \tag{44}$$

where $LW^{\uparrow}$, LH, and SH are the linearized surface fluxes.

Representing each soil layer with the fluxes of energy into and out of that soil layer results in a tri-diagonal matrix which we solve using the Thomas Algorithm. We start at the bottom of the soil column and sweep up the matrix to solve for an initial estimate of surface temperature T_s. If there is no snow on the ground, or if there is snow on the ground, but T_s is below freezing, that T_s is used to complete the downwards sweep of the matrix and calculate the remaining soil temperatures. If the estimated surface temperature is above freezing and there is snow on the ground, the surface temperature is set to 0°C, and the difference between the predicted surface temperature and 0°C is used to melt snow. If there is still snow left after all the energy from the temperature difference is used, the surface temperature is kept at 0°C, and the downwards sweep of the matrix is used to calculate the temperature of the remaining soil layers. If there is enough energy associated with the difference in the predicted surface temperature and 0°C, all the snow is melted and the remaining energy is converted back to a temperature to calculate a modified T_s, which is then used to solve for the remaining soil temperatures. This representation of snow melt is comparable to that used in the LM2 model [Anderson et al., 2004]. The energy used to melt snow is saved as G_{snow} = snowmelt $\times$ h_{fus}. A similar procedure is used to calculate the temperature profile of glaciated gridcells, but using the thermal properties of ice rather than soil.

After the soil temperatures have been calculated, we set the temperature of the top soil layer to be the surface temperature T_s (the topmost soil layer is very thin).

1.4.4 Water Accounting

Water enters the bucket via either rain (liquid precipitation) or snow melt. The bucket has a prescribed capacity; by default, the bucket capacity is 200 kg/m^2 (as in the LM2 code [Anderson et al., 2004]), but this can be modified to vary spatially by the user. Water can leave the bucket through evaporation (latent heat flux) or runoff (if the bucket exceeds capacity).

Snow accumulation is unlimited. Snow is added to the snow ‘bucket’ via snowfall (frozen precipitation) from the atmosphere. Snow can leave the snow bucket via either sublimation (directly to the atmosphere) or snow melt (to the water bucket on the land). Because snow accumulation is not limited by any ‘capacity’, this has the consequence that over glaciated regions, snow can accumulate indefinitely. Because the land/atmosphere/slab-ocean system does not conserve water, this is not a problem (the atmosphere doesn’t see any physical height to the snow), but if a dynamic ocean were used, a calving-scheme would need to be implemented to deposit ice into the ocean at high latitudes. This is similar to the implementation of snow in LM2 [Anderson et al., 2004].

1.5 Model behavior comparison with CLM

To demonstrate the general behavior of SLIM, we present a comparison of SLIM with CLM5 [Lawrence et al., 2018], forced with GSWP3 reanalysis data, repeating the data from year 2001-2010 for 50 years. Results shown are the average of the last 30 years of the simulations (allowing 20 years of model spin-up). We also compare the last 30 years of coupled simulations with SLIM and CLM5 coupled to the Community Atmosphere Model v5 (CAM5) [Neale et al., 2012], a slab ocean model (SOM) [Neale et al., 2012], and the Los Alamos Sea Ice Model for interactive sea ice (CICE5) [Hunke et al., 2013, LANS, 2017]. CLM is run in bgc mode (interactive biogeochemistry) with an 1850 map of vegetation. The pattern of vegetation height for SLIM is derived from the last 30 years of the CLM5 simulation. The pattern of evaporative resistance is derived from the stomatal conductance, saved from the CLM5 simulation. The stomatal conductance in CLM5 is calculated separately for sunlit and shaded leaves; we weight the conductance by the leaf area of sunlit and shaded leaves then convert to units of resistance. The four streams of radiation impacted by surface albedo (visible/near-infrared direct/diffuse) are calculated from the summertime surface albedo of CLM5 (to avoid imposing any pattern of seasonal snow cover). Gridcells which have over 50% glacier cover in CLM5 are defined as glaciers in SLIM, and thus use the thermal properties of ice and albedo of snow. Unless explicitly stated, we compare the results of the offline simulations rather than the coupled land-atmosphere simulations.

Only summertime conductance and albedo values are used for each hemisphere (June, July, August in the Northern Hemisphere, and December, January, February in the Southern Hemisphere), but the resulting maps of surface conductance and albedo are fixed throughout the year in the SLIM simulations, while the CLM albedo can vary as leaf area and soil moisture change.

Snow cover can modify this base-line albedo throughout the year in both SLIM and CLM5, but the snow-free albedo in the SLIM simulations has no seasonal cycle, nor does the evaporative resistance. The snow-masking depth is fixed to 50 kg/m^2 everywhere in this SLIM simulation (and is not a function of vegetation height, as it is in CLM).

As such, we do not expect SLIM to produce a surface climate identical to that of CLM; rather, we demonstrate that even with this fairly crude approximation of the vegetation patterns of CLM, SLIM can still produce surface temperatures and fluxes comparable to those from the much more complex CLM.

The annual mean temperature of SLIM is comparable to that of CLM in most regions (figure 2). Portions of the northern high latitudes are over 1K cooler in SLIM than CLM, largely due to SLIM having a much brighter snow albedo over non-glaciated regions. Over the interior of Antarctica, sensible heat fluxes are slightly (10 W/m^2) too high and longwave fluxes are too low (figure 3). Albedo differences along the Antarctic coast (non-glaciated regions, where albedo is calculated as a combination of ground albedo and snow) additionally contribute to differences in surface temperature and surface energy fluxes.

Parts of the tropics and mid-latitudes are too hot (notably the Saraha/Sahel region of Africa, and the Tibetan plateau; figure 2). Over the Tibetan plateau, SLIM has a lower albedo (is darker), contributing to the warmer surface temperatures (figure 4). Over the Sahara, sensible heat fluxes are too low (perhaps because of surface roughness differences) resulting in warmer surface temperatures. In sub-saharan Africa, indeed in most of the tropics, latent heat fluxes are much lower than in CLM, which are roughly compensated for by sensible heat fluxes which are higher than in CLM (figure 3). That is, with the maps of surface properties used in this simulation of SLIM, the evaporative fraction is much lower than that of CLM.

In the coupled land-atmosphere simulations, the temperature anomalies between SLIM and CLIM increase substantially. In particular, parts of the tropics and mid-latitudes in the SLIM-CAM5 simulations are up to 3K warmer than the CLM5-CAM5 simulations, while parts of the Arctic are 1-3K cooler in SLIM-CAM5 than CLM5-CAM5. However, the temperature difference over other areas, specifically Antarctica, improve in the coupled simulations.

Seasonal cycles are shown for four locations with very different climates: the Sahara, the Amazon, Siberia, and the Great Plains (figure 5). The seasonal cycle of temperature is very similar between SLIM and CLM (figure 6), as the seasonal temperature differences driven by the atmospheric forcing data are much larger than the difference in temperature produced by the land models themselves. The differences between SLIM and CLM in individual terms of the surface energy budget are much larger than the differences in temperature, mostly coming from a difference in evaporative fraction: when latent heat flux in SLIM is lower than in CLM, sensible heat flux tends to be higher (figure 7).

The seasonal cycle of soil temperatures is physically consistent with our intuition (figure 8). In all areas, the peak in surface soil temperatures occurs in summer, with the peak in deep soil temperatures lagging. Deep soils are cooler than surface soils in summer, and warmer than surface soils in winter, as we would expect, with the ground taking up heat during warm summer months and releasing heat during cold winter months. The soil properties of all non-glaciated land areas in SLIM are identical in this simulation. The diurnal temperature profile of soil temperatures is also consistent with our physical expectation, with surface soil temperatures having a large diurnal temperature cycle and deep soils having no diurnal temperature cycle, and surface soil temperatures peak a few hours after local noon (figure 9).

SLIM executes over 98% faster than CLM.

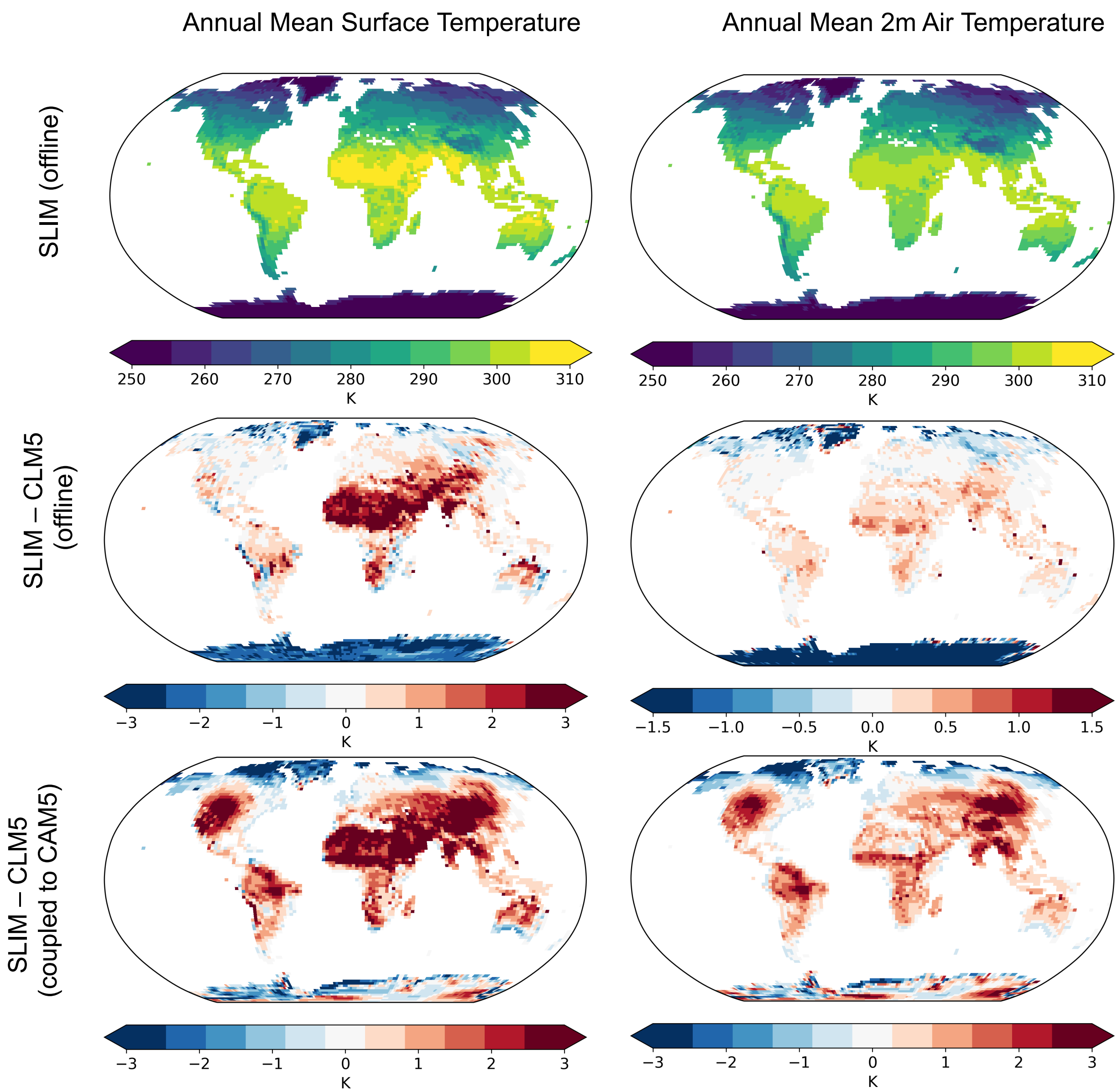

Figure 2: Annual mean surface radiative skin temperature (left) and 2m air temperature (right) in the SLIM model run offline (top row), the difference between offline SLIM and CLM5 (middle row), and the difference between SLIM and CLM5 when coupled to CAM5.

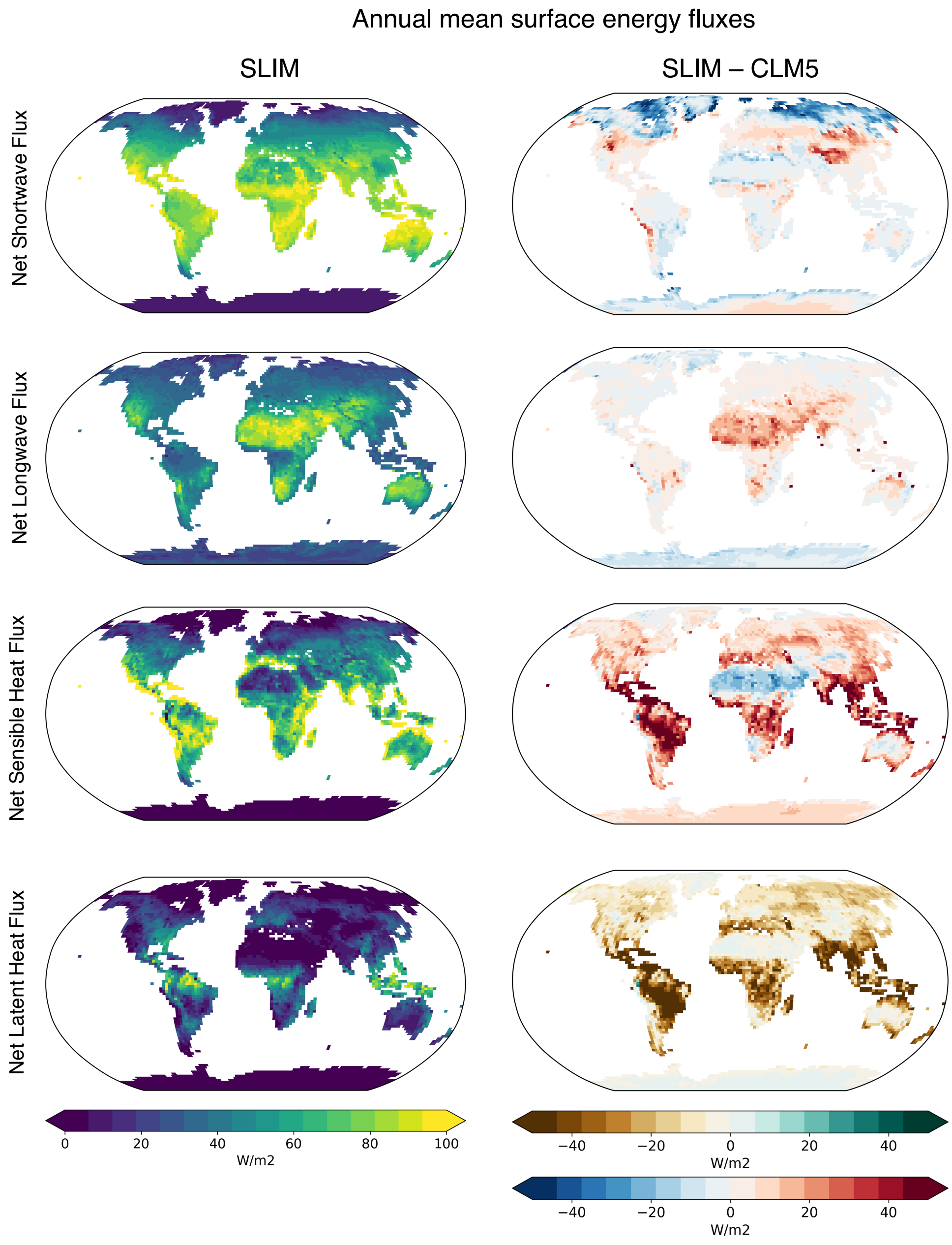

Figure 3: Annual mean surface energy budget: net flux of shortwave raidation (row 1), net flux of longwave radiation (row 2), sensible heat flux (row 3), and latent heat flux (row 4) for the offline SLIM model (left column), and the difference between offline SLIM and CLM5 (right column).

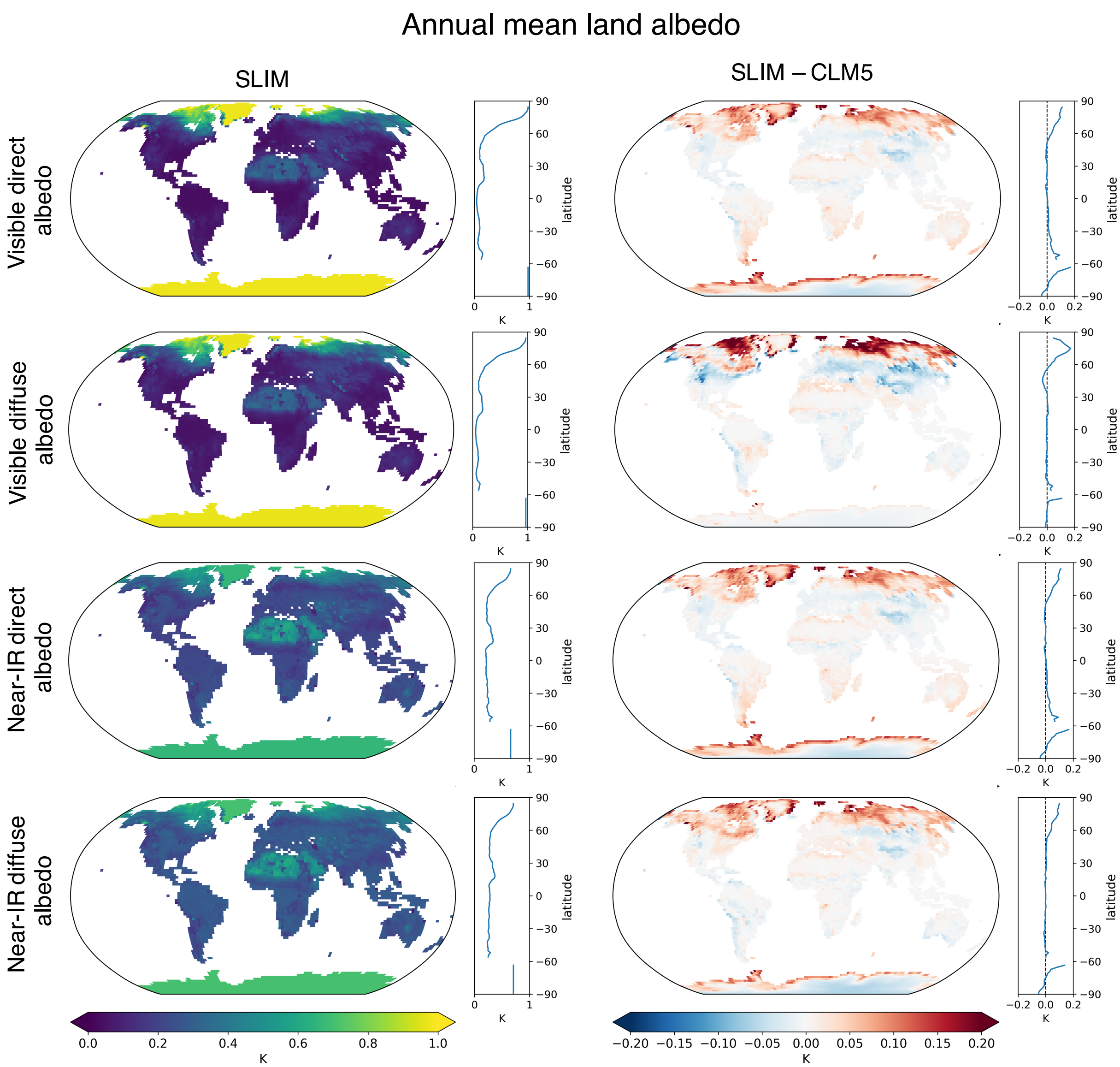

Figure 4: Annual mean land albedo for visible direct radiation (row 1), visible diffuse radiation (row 2), near-infrared direct radiation (row 3), and near-infrared diffuse radiation (row 4) for the offline SLIM model (left column), and the difference between offline SLIM and CLM5 (right column).

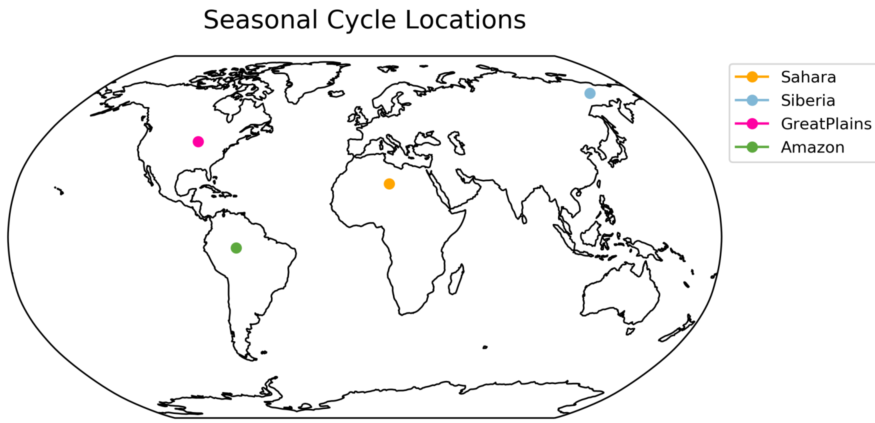

Figure 5: Locations used for seasonal cycle plots: Sahara: 23.7°N, 12.5°E (orange); Siberia: 65.4°N, 150°E (blue); Great Plains: 42.6°N, 92.5°W (pink); Amazon: 4.7°S, 65°W (green).

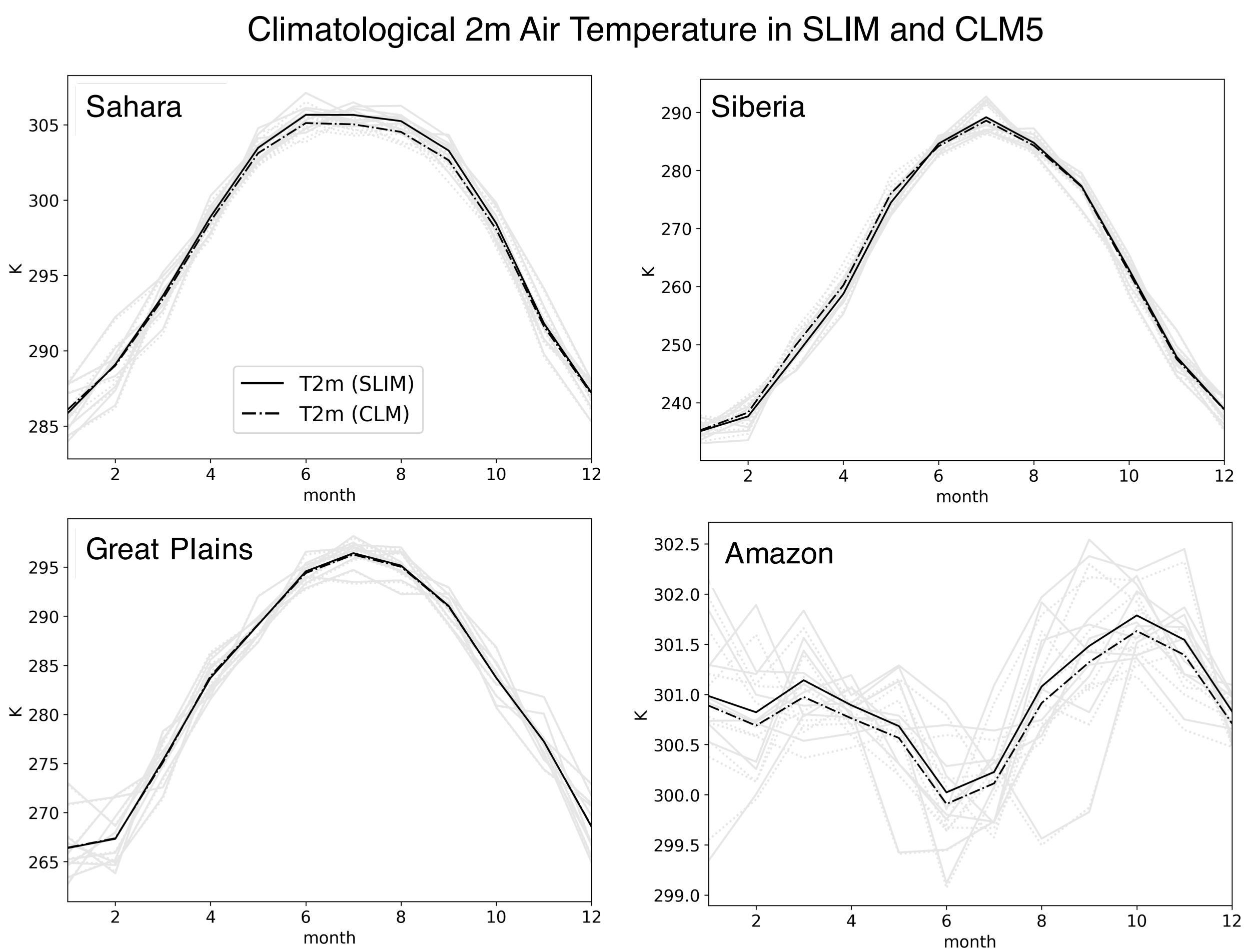

Figure 6: Seasonal cycle of 2m air temperature [K] over 4 locations in SLIM (solid lines) and CLM5 (dash-dot lines). The climatological cycle is shown in black lines, while individual years are show in gray.

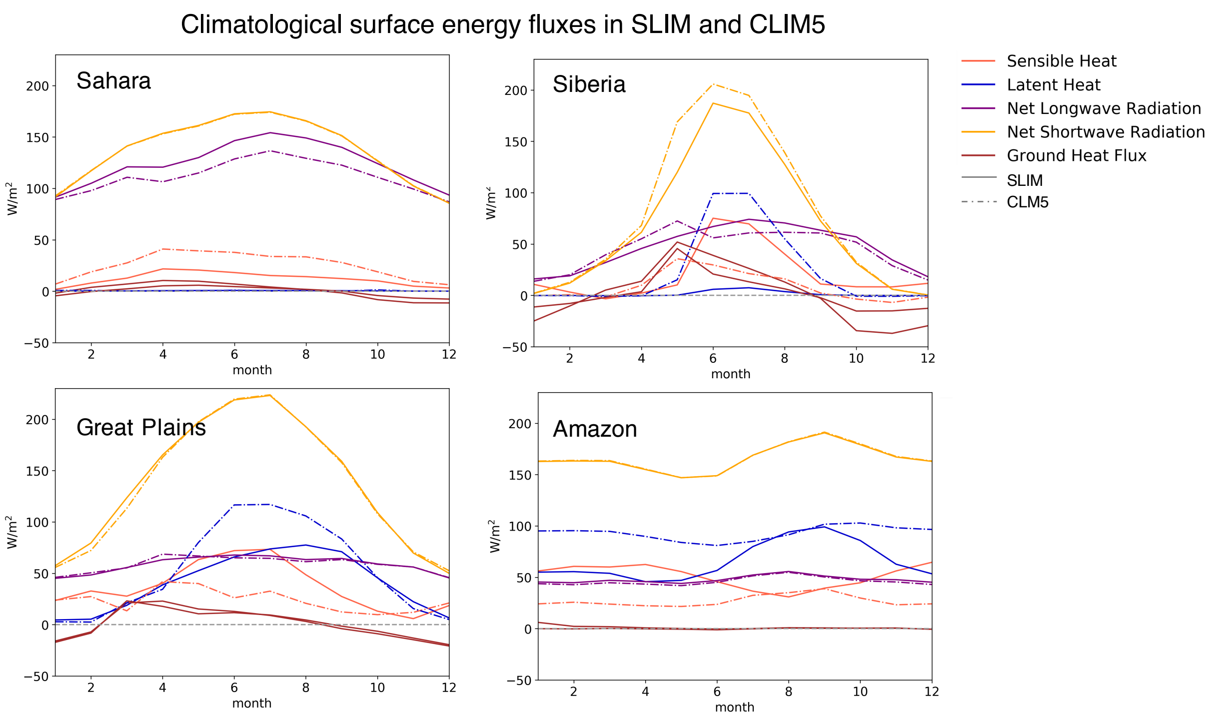

Figure 7: Seasonal cycle of the individual terms of the surface energy budget [W/m^2] over 4 locations in SLIM (solid lines) and CLM5 (dash-dot lines). The net flux of shortwave radiation (absorbed shortwave) is shown in yellow; net longwave radiation (positive upwards) is shown in purple; sensible heat (positive upwards) is shown in red; latent heat (positive upwards) is shown in blue; ground heat flux (heat uptake by soil or snow) is shown in brown.

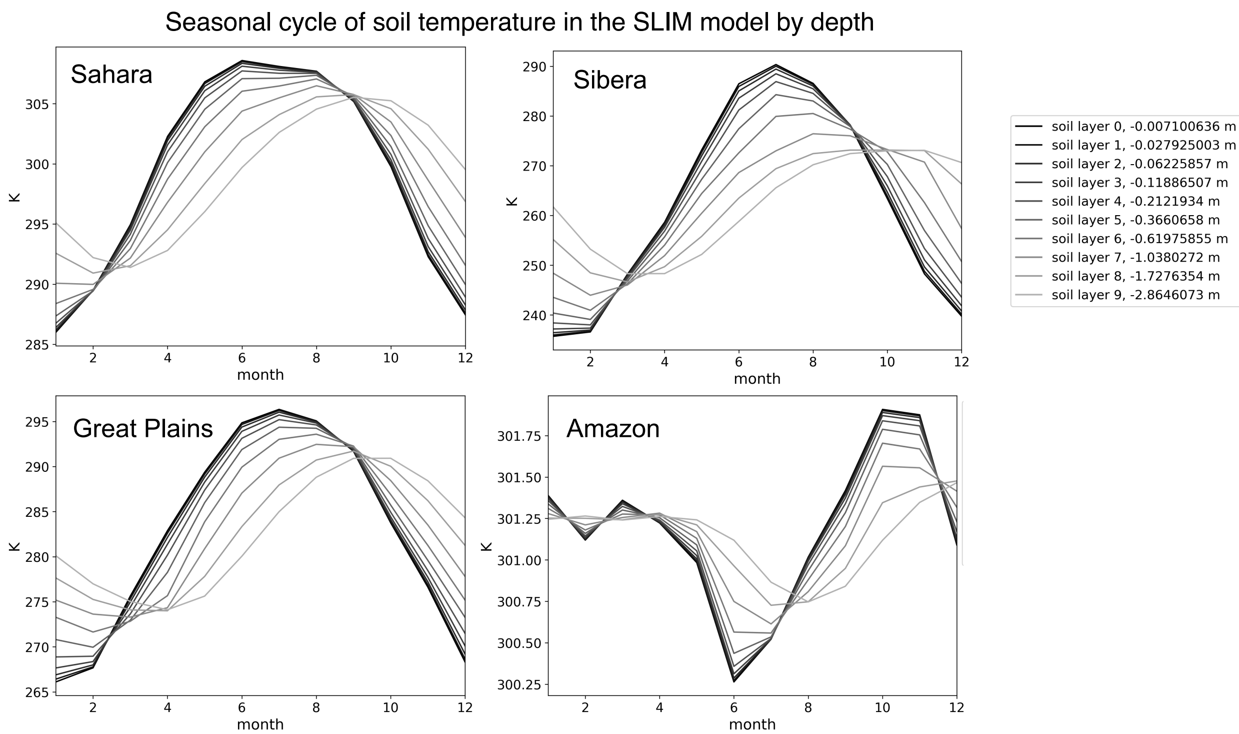

Figure 8: Seasonal cycle of soil temperature over 4 locations in SLIM, as a function of soil depth (darker lines are closer to the surface, lighter lines are deeper in the soil).

Prescribed Land Properties			
Variable	Typical Value	Units	Description
α_{gvd}	0.2	[unitless]	Visible direct albedo for bare ground.
α_{svd}	0.8	[unitless]	Visible direct albedo for deep snow.
α_{gnd}	0.3	[unitless]	Near-infrared direct albedo for bare ground.
α_{snd}	0.6	[unitless]	Near-infrared direct albedo for deep snow.
α_{gvf}	0.2	[unitless]	Visible diffuse albedo for bare ground.
α_{svf}	0.8	[unitless]	Visible diffuse albedo for deep snow.
α_{gnf}	0.3	[unitless]	Near-infrared diffuse albedo for bare ground.
α_{snf}	0.6	[unitless]	Near-infrared diffuse albedo for deep snow.
M_s	50	[kg/m^2]	Snow-masking depth: mass of water required in snow bucket to fully mask the bare ground albedo.
r_s	100	[s/m]	"Lid" resistance to evaporation
W_{max}	200	[kg/m^2] $=$ [mm]	Bucket capacity: maximum amount of water the soil can hold
h_c	0.1-20.0	[m]	Vegetation height; used to calculate roughness lengths for momentum and heat.
$emissivity$	0.9-1.0	[unitless]	Surface emissivity for longwave radiation
glc_{mask}	logical	[unitless]	Mask marking gridcells which should be treated as glaciers/ice sheets.
$soil_{tk,1d}$	1.5	[W/m/K]	Thermal conductivity of soil (used for whole column).
$soil_{cv,1d}$	2.0e6	[J/m3/K]	Heat capacity of soil (used for whole column).
$glc_{tk,1d}$	2.4	[W/m/K]	Thermal conductivity of ice (used for whole column where glaciated).
$glc_{cv,1d}$	1.9e6	[J/m3/K]	Heat capacity of ice (used for whole column where glaciated).

Table 1: Typical values for each of the model parameters in SLIM.

Information required from atmosphere		
Variable	Units	Description
$SW^{\downarrow}_{nd}$	[W/m^2]	Direct, near-infrared incident solar radiation
$SW^{\downarrow}_{vd}$	[W/m^2]	Direct, visible incident solar radiation
$SW^{\downarrow}_{ni}$	[W/m^2]	Diffuse, near-infrared incident solar radiation
$SW^{\downarrow}_{vi}$	[W/m^2]	Diffuse, visible incident solar radiation
$LW^{\downarrow}$	[W/m^2]	Downwelling longwave radiation
z_{ref}	[m]	height of reference level for atmospheric variables given at reference height
T_{bot}	[K]	Temperature at lowest level of atmosphere
θ_{ref}	[K]	Potential temperature at reference height
q_{bot}	[kg/kg]	Specific humidity at lowest level of atmosphere
u_{ref}	[m/s]	Wind speed at reference height
e_{ref}	[Pa]	Vapor pressure at reference height
p_{bot}	[Pa]	Atmospheric pressure at lowest level of atmosphere
p_{srf}	[Pa]	Surface pressure
ρ_{air}	[kg/m^3]	Density of air at reference height
c_p	[J/kg/K]	Specific heat of air at constant pressure at reference height
$rain$	[m/s]	liquid precipitation
$snow$	[m/s]	frozen precipitation

Table 2: Table of values from the atmospheric model (or data atmosphere) required by the land model.

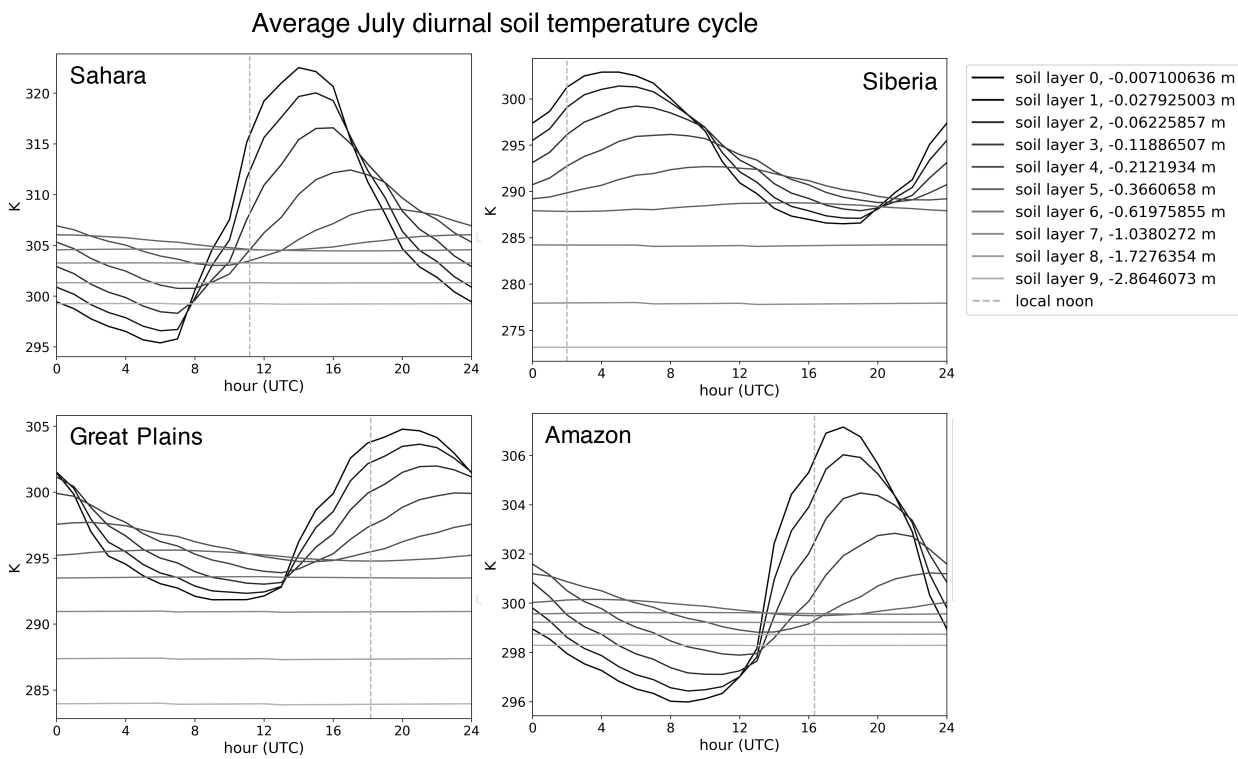

Figure 9: Diurnal cycle of soil temperature (averaged over all July days in a single year) over 4 locations in SLIM, as a function of soil depth (darker lines are closer to the surface, lighter lines are deeper in the soil). Local noon is indicated by the vertical dashed gray line.

2 Non-linear response to surface roughness

Initial simulations exploring the response of surface fluxes to vegetation height (using h_c = 0.1, 1.0, and 10.0 m) showed a distinctly non-linear response of surface temperature and surface energy fluxes to changes in vegetation height. This is in contrast to the linear response of surface temperatures and energy fluxes to incremental changes in albedo and evaporative resistance. To explore this further, we performed additional experiments with vegetation heights of h_c = 2.0, 5.0, and 20.0 m, and found that the response is qualitatively similar to a negative exponential (supplemental figure 15). To proceed with our linear approximation of the response, we separate the response to vegetation height into two distinct regimes - that of 'short' vegetation ($\leq$ 2m) and that of 'tall' vegetation ($\geq$ 2m); this roughly corresponds to one relationship for grasses to shrubs and small trees, and second relationship for tall trees. We chose 2m as the separation point by calculating vegetation height associated with the maximum change in the slope of the change in surface temperature between consecutive vegetation height experiments for each non-glaciated land point, then taking the mean of the resulting vegetation heights. The resulting vegetation height with on average the largest change in the slope of the temperature response to changing vegetation height was approximately 1.5 m. So, we calculate one slope for the three experiments with h_c = 0.1, 1.0, and 2.0 m, and a separate slope for the four experiments with h_c = 2.0, 5.0, 10.0, and 20.0 m.

The response of surface temperatures to incremental changes in short vegetation is much stronger than the response of surface temperatures to incremental changes in tall vegetation. The scaling factors applied to the slope of the temperature response (ie, the scaling factor that leads to roughly 1K maximum warming per incremental vegetation height change) are a 0.5 m decrease in vegetation height for the short vegetation regime, and a 10.0 m decrease in vegetation height for the tall vegetation regime. However, the overall patterns (though not magnitudes) of surface temperature response to decreased vegetation height are similar both between the short and tall response regime, and between the coupled and offline simulations (supplemental figure 16).

3 Supplemental Figures

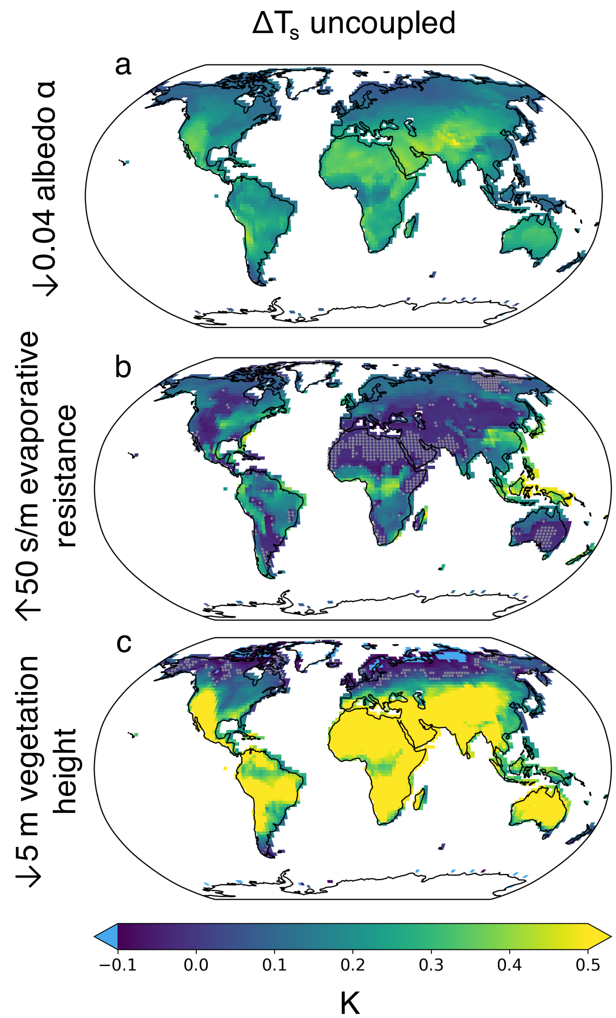

Figure 10: Surface temperature response to changing surface properties, but with a smaller range to better show spatial pattern of temperature response in offline simulations only. Annual mean scaled surface temperature T_s response [K] for the offline simulations, per 0.04 darkening of the surface albedo (a), 50 s/m increase in evaporative resistance (b), and 5.0 m decrease in vegetation height (c). Cyan regions ($\Delta T_s < 0.1$) indicate regions where the temperature cooled substantially in response to the prescribed surface change.

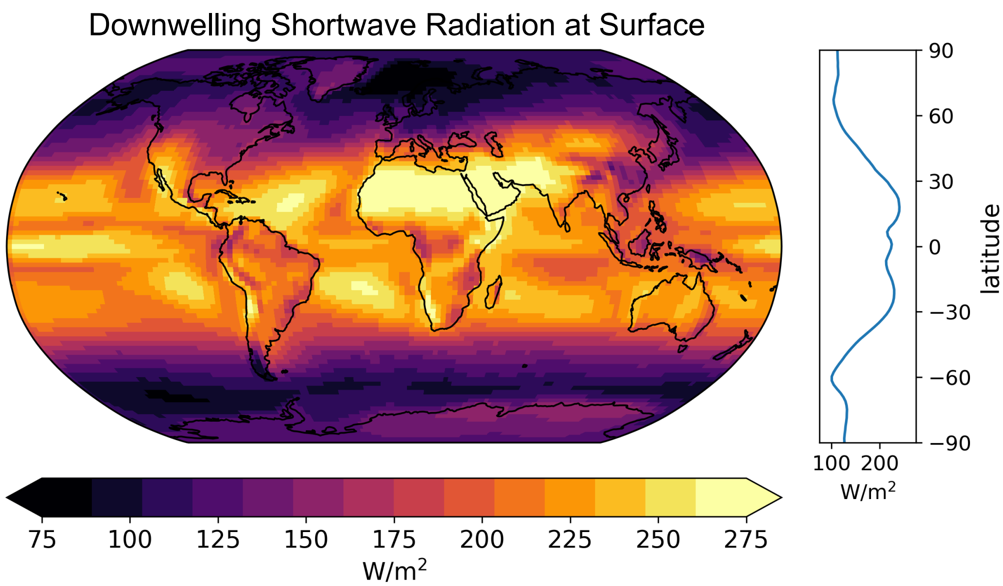

Figure 11: Annual mean downwelling shortwave radiation at the surface [W/m^2] in the 'baseline' idealized simulation (albedo = 0.2, evaporative resistance = 50 s/m, vegetation height = 0.1 m), with SLIM coupled to CAM5.

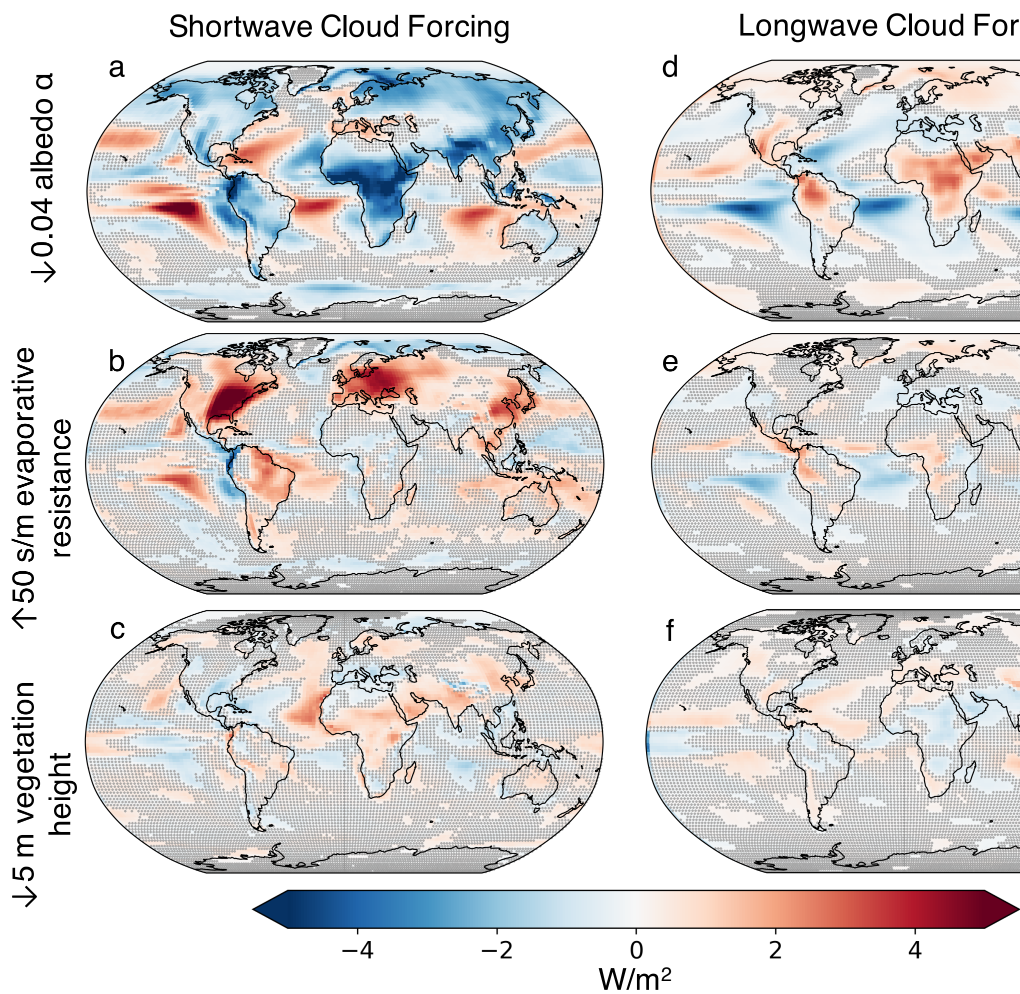

Figure 12: Change in shortwave cloud forcing (left) and longwave cloud forcing (right) per 0.04 decrease in albedo (a,d), 50 s/m increase in evaporative resistance (b,e), and 5 m decrease in vegetation height (c,f). Stippling indicates statistically insignificant regions ($p > 0.05$). The shortwave and longwave cloud forcing are calculated by the model, and are equal to the difference in radiation reaching the surface between a sky that includes the radiative effects of clouds, and a 'clear' (cloud-free) sky.

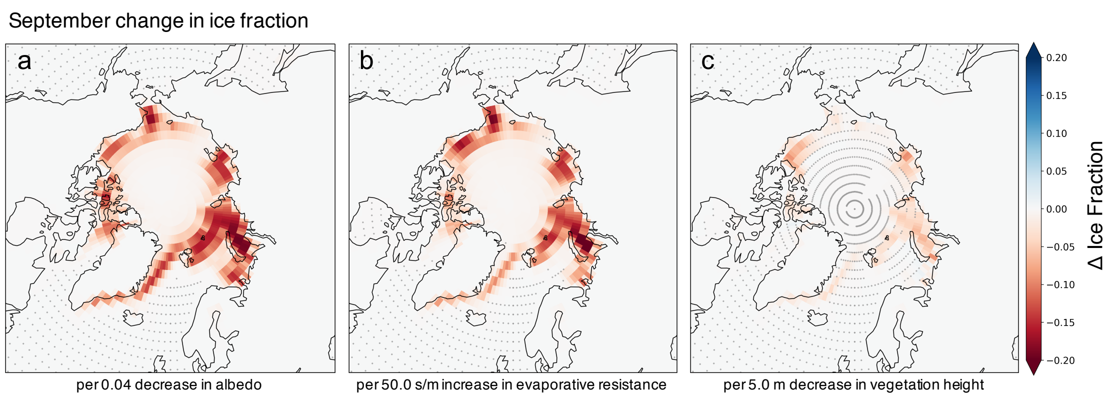

Figure 13: Change September ice fraction per (a) 0.04 decrease in land albedo, (b) 50 s/m increase in land surface evaporative resistance, and (c) 5m decrease in land surface vegetation height. Stippling indicates regions which are not significant ($p > 0.05$).

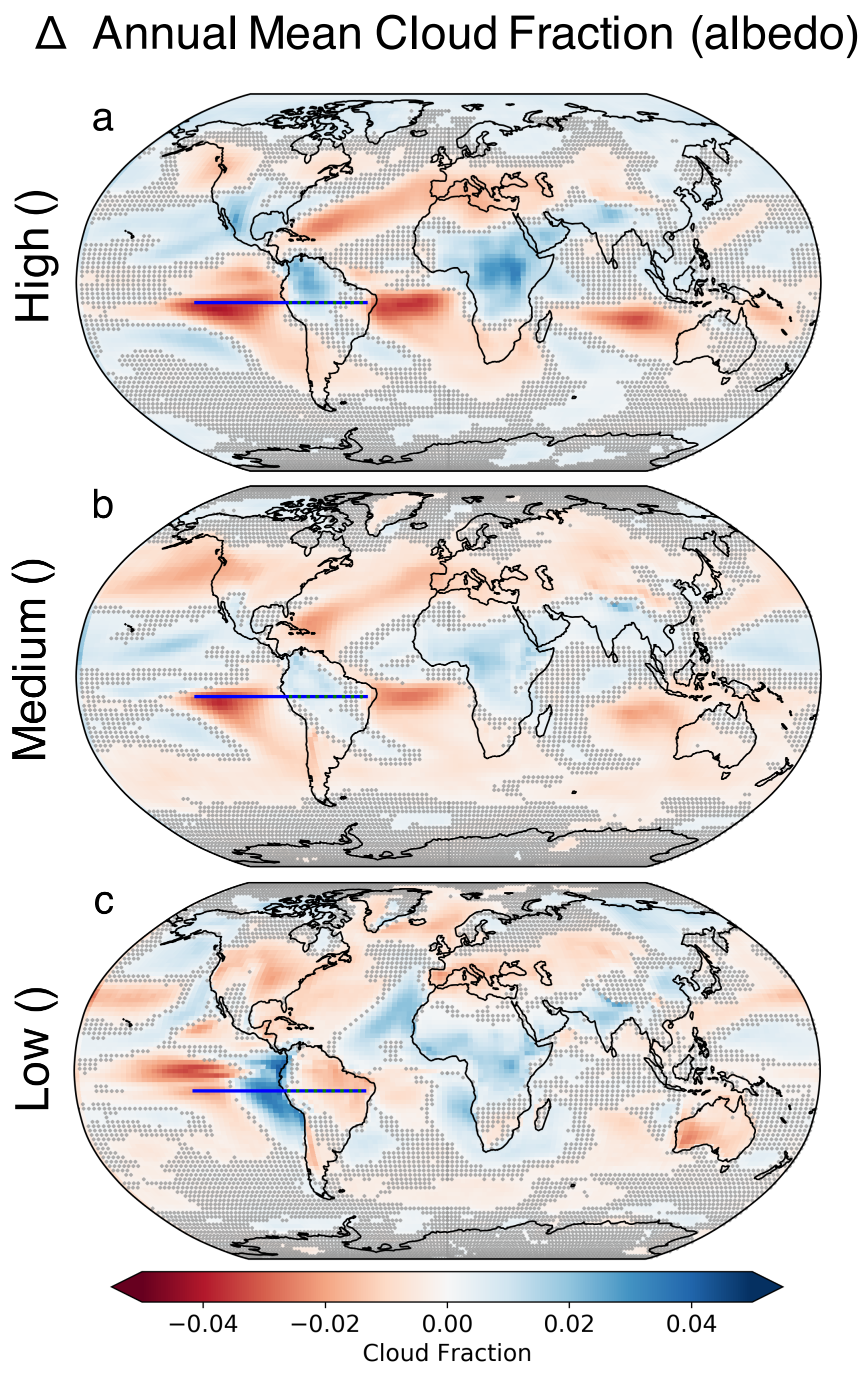

Figure 14: Annual mean change in cloud fraction per 0.04 decrease in surface albedo for (a) high (400 hpa - top of model), (b) medium (700-400 hpa) and (c) low (surface - 700 hpa) clouds per 0.4 decrease in surface albedo. Stippling indicates insignificant changes with p>0.05. Horizontal blue lines show the region where subsidence was analyzed (not shown).

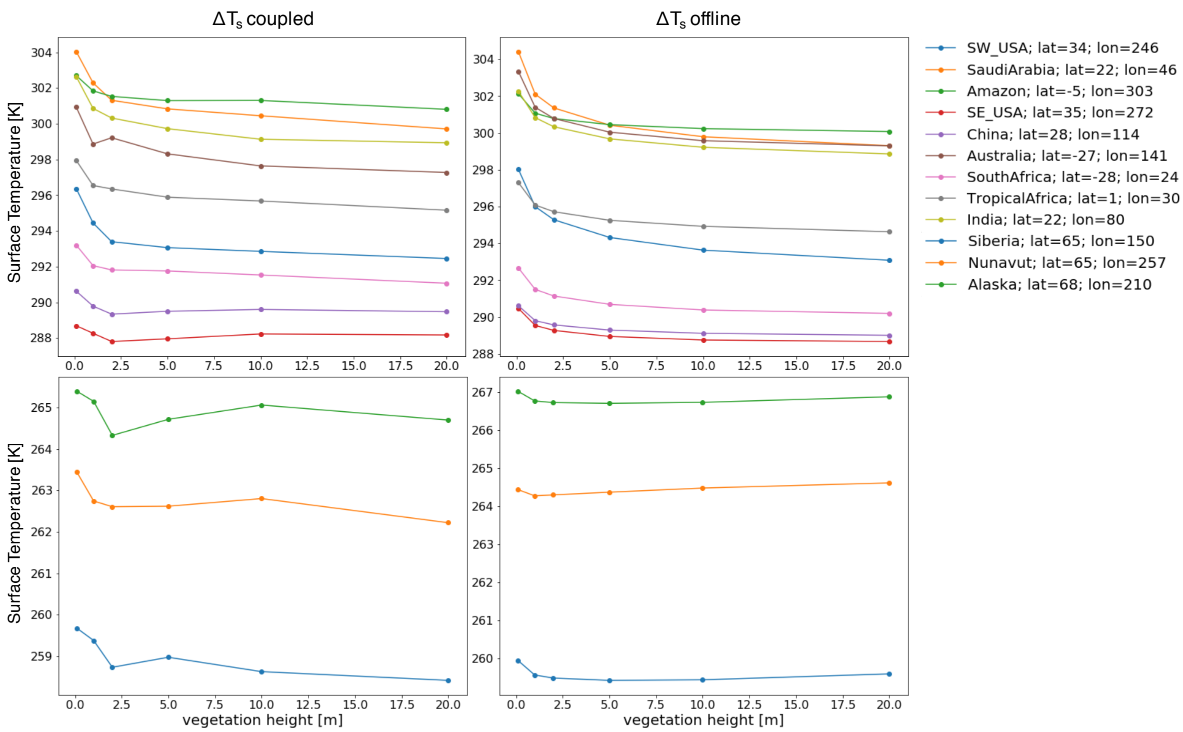

Figure 15: The annual mean surface temperature at select locations across the range of vegetation height experiments, with h_c = 0.1, 1.0, 2.0, 5.0, 10.0, and 20.0 m. Coupled simulations are shown in the left column, while offline simulations are shown in the right column. Mid and low latitude locations are shown in the top row, while high latitude locations are shown in the bottom row (not differing y-axis ranges). The latitude (positive for Northern hemisphere, negative for Southern hemisphere) and longitude locations (increasing Eastward from 0 to 360) are given for each location in the legend.

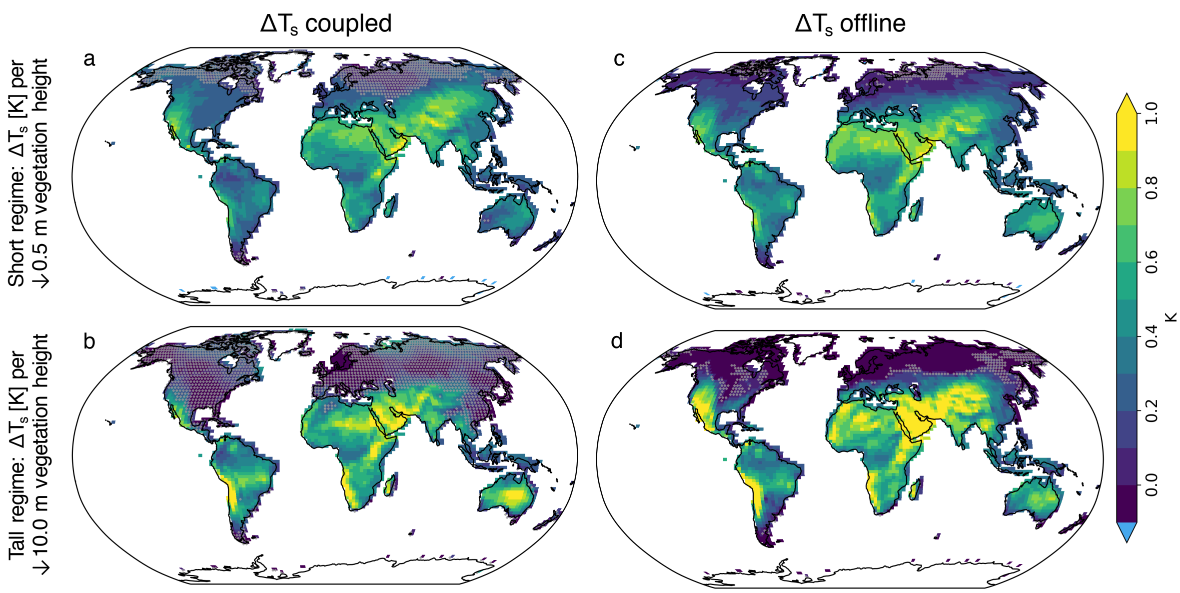

Figure 16: Change in surface temperature in the coupled (left) and offline (right) simulations for the short (top row) and tall (bottom row) vegetation height regimes. The short regime is scaled by a 0.5 m decrease in vegetation height, while the tall regime is scaled by a 10.0 m decrease in vegetation height. Stippled regions do not pass a t-test with p=0.05.

References

Anderson, J. L., Balaji, V., Broccoli, A. J., Cooke, W. F., Delworth, T. L., Dixon, K. W., Donner, L. J., Dunne, K. a., Freidenreich, S. M., Garner, S. T., Gudgel, R. G., Gordon, C. T., Held, I. M., Hemler, R. S., Horowitz, L. W., Klein, S. a., Knutson, T. R., Kushner, P. J., Langenhost, A. R., Lau, N. C., Liang, Z., Malyshev, S. L., Milly, P. C. D., Nath, M. J., Ploshay, J. J., Ramaswamy, V., Schwarzkopf, M. D., Shevliakova, E., Sirutis, J. J., Soden, B. J., Stern, W. F., Thompson, L. a., Wilson, R. J., Wittenberg, A. T., and Wyman, B. L. (2004). The new GFDL global atmosphere and land model AM2-LM2: Evaluation with prescribed SST simulations. *Journal of Climate*, 17(24):4641–4673.

Bonan, G. B. (1996). Ecological , Hydrological , and Atmospheric Studies : Technical Description and User ' S Guide.

Bonan, G. B. (2002). *Ecological climatology: concepts and applications*. Cambridge University Press, 1 edition.

Dickinson, R. E., Henderson-Sellers, A., Kennedy, P. J., Dickinson, E., Henderson-Sellers, A., and Kennedy, J. (1993). Biosphere-atmosphere Transfer Scheme (BATS) Version 1e as Coupled to the NCAR Community Climate Model. *NCAR Tech. Rep. NCAR/TN-3871STR, 72*, (August):77.

Hunke, E. C., Lipscomb, W. H., Turner, A. K., Jeffery, N., and Elliott, S. (2013). CICE : the Los Alamos Sea Ice Model Documentation and Software User ' s Manual LA-CC-06-012. page 115.

Hurrell, J. W., Holland, M. M., Gent, P. R., Ghan, S., Kay, J. E., Kushner, P. J., Lamarque, J. F., Large, W. G., Lawrence, D., Lindsay, K., Lipscomb, W. H., Long, M. C., Mahowald, N., Marsh, D. R., Neale, R. B., Rasch, P., Vavrus, S., Vertenstein, M., Bader, D., Collins, W. D., Hack, J. J., Kiehl, J., and Marshall, S. (2013). The community earth system model: A framework for collaborative research. *Bulletin of the American Meteorological Society*, 94(9):1339–1360.

LANS (2017). CICE5. Technical report, Los Alamos National Security, LLC (LANS).

Lawrence, D., Fisher, R., Koven, C., Oleson, K., Swenson, S., Vertenstein, M., Ben, Andre, B., Bonan, G., Ghimire, B., van Kampenhout, L., Kennedy, D., Kluzek, E., Knox, R., Lawrence, P., Li, F., Li, H., Lombardozzi, D., Lu, Y., Perket, J., Riley, W., Sacks, W., Shi, M., Wieder, W., and Xu, C. (2018). Technical Description of version 5.0 of the Community Land Model (CLM). Technical report, National Center for Atmospheric Research, Boulder, Colorado.

Manabe, S. (1969). Climate and the Ocean Circulation 1. *Monthly Weather Review*, 97(11):739–774.

Milly, P. C. D. and Shmakin, a. B. (2002a). Global Modeling of Land Water and Energy Balances. Part I: The Land Dynamics (LaD) Model. *Journal of Hydrometeorology*, 3(3):283–299.

Milly, P. C. D. and Shmakin, a. B. (2002b). Global Modeling of Land Water and Energy Balances. Part I: The Land Dynamics (LaD) Model. *Journal of Hydrometeorology*, 3(3):283–299.

Monin, A. S. and Obukhov, A. M. (1954). Basic laws of turbulent mixing in the surface layer of the atmosphere. *Contrib. Geophys. Inst. Acad. Sci. USSR*, 24(151):163–187.

Neale, R. B., Gettelman, A., Park, S., Chen, C.-C., Lauritzen, P. H., Williamson, D. L., Conley, A. J., Kinnison, D., Marsh, D., Smith, A. K., Vitt, F., Garcia, R., Lamarque, J.-F., Mills, M., Tilmes, S., Morrison, H., Cameron-smith, P., Collins, W. D., Iacono, M. J., Easter, R. C., Liu, X., Ghan, S. J., Rasch, P. J., Taylor, M. a., Gettelman, A., Lauritzen, P. H., Park, S., Williamson, D. L., Conley, A. J., Garcia, R., Kinnison, D., Lamarque, J.-F., and Others (2012). Description of the NCAR community atmosphere model (CAM 5.0). *NCAR Tech. Note NCAR/TN-486+STR*.

Paterson, W. S. B. (1994). *The physics of glaciers*. Pergamon, Oxford, OX, England; Tarrytown, N.Y., U.S.A., 3 edition.